

1 Fluorescence characteristics, absorption properties, and 2 radiative effects of water-soluble organic carbon in 3 seasonal snow across northeastern China

4 Xiaoying Niu¹, Wei Pu¹, Pingqing Fu², Yang Chen¹, Yuxuan Xing¹, Dongyou Wu¹,
5 Ziqi Chen¹, Tenglong Shi¹, Yue Zhou¹, Hui Wen¹, Xin Wang^{1,2}

6 ¹Key Laboratory for Semi-Arid Climate Change of the Ministry of Education, College of Atmospheric
7 Sciences, Lanzhou University, Lanzhou 730000, China

8 ²Institute of Surface-Earth System Science, Tianjin University, Tianjin 300072, China

9 *Correspondence to:* Xin Wang (wxin@lzu.edu.cn)

10 **Abstract.** Although water-soluble organic carbon (WSOC) in the cryosphere can significantly influence
11 the global carbon cycle and radiation budget, WSOC in the snowpack has received little scientific
12 attention to date. This study reports the fluorescence characteristics, absorption properties, and radiative
13 effects of WSOC based on 34 snow samples collected from sites in northeastern China. Sampling sites
14 were divided into five groups, comprising southeastern Inner Mongolia (SEIM), northeastern Inner
15 Mongolia (NEIM), the south of northeastern China (SNC), the north of northeastern China (NNC), and
16 the Changbai Mountain area (CBM). Together, these groups represent a significant degree of regional
17 WSOC variability, with concentrations ranging from 0.5 ± 0.2 to $5.7 \pm 3.7 \mu\text{g g}^{-1}$ (mean = $3.6 \pm 3.2 \mu\text{g}$
18 g^{-1}). We then identified the three principal fluorescent components of WSOC as (1) a high-oxygen
19 humic-like substance (HULIS-1) of terrestrial origin, (2) a low-oxygen humic-like substance (HULIS-2)
20 of mixed origin, (3) and a protein-like substance (PRLIS) derived from autochthonous microbial activity.
21 In SEIM, a region dominated by desert and exposed soils, the WSOC content exhibits the highest
22 humification index (HIX) but the lowest fluorescence (FI) and biological (BIX) indices; the fluorescence
23 signal is mainly attributed to HULIS-1, and thus implicates soil as the primary source. By contrast, the
24 HIX (FI and BIX) value was the lowest (highest) and PRLIS most intense in the remote grasslands and
25 forested areas of NEIM, suggesting a primarily biological source. For SNC and NNC, both of which are

1 characterized by intensive agriculture and industrial activity, the fluorescence signal is dominated by
2 HULIS-2 and the HIX, FI, and BIX values are all moderate, indicating mixed origins for WSOC
3 (anthropogenic activity, microbial activity, and soil). We also observed that, throughout northeastern
4 China, the light absorption of WSOC is dominated by HULIS-1, followed by HULIS-2 and PRLIS. The
5 contribution of WSOC to albedo reduction (average concentration $3.6 \mu\text{g g}^{-1}$) in the ultraviolet–visible
6 (UV–vis) band is approximately half that of black carbon (BC: average concentration $0.6 \mu\text{g g}^{-1}$);
7 radiative forcing is $3.8 (0.8) \text{ W m}^{-2}$ in old (fresh) snow, equating to 19 % (17 %) of the radiative forcing
8 of BC. These results indicate that WSOC has a profound impact on snow albedo and the solar radiation
9 balance.

10 **1 Introduction**

11 Seasonal snow plays a significant role in Earth’s solar radiation energy budget owing to its high
12 reflectivity (Beniston et al., 2017; Usha et al., 2020; Xie et al., 2018). In recent decades, however, the
13 extent of snow-covered areas has trended downward, partially as a result of the presence of light-
14 absorbing particles (LAPs) in the snowpack (Barnett et al., 2008; Groisman et al., 1994; Dumont et al.,
15 2014). The LAPs in seasonal snow, such as black carbon (BC), organic carbon (OC), mineral dust (MD),
16 and biota (Beres et al., 2020; Di Mauro, 2020; Els et al., 2020; Qian et al., 2015; Wu et al., 2016), can
17 strongly absorb solar radiation, which together serves to lower surface albedo and impose a positive
18 radiative forcing (Cui et al., 2021; Dumont et al., 2014; Hansen and Nazarenko, 2004; Shi et al., 2022b;
19 Warren and Wiscombe, 1980; Zhang et al., 2017). Ultimately, LAPs can accelerate snow melting (Li et
20 al., 2021b) and disturb the global radiative balance, therefore, have important implications for regional
21 and global climate change (Skiles et al., 2018; Shi et al., 2022a).

1 Snowpack BC and MD have been the focus of considerable research in snow-covered regions worldwide
2 (Li et al., 2021a; Zhang et al., 2018; Antony et al., 2014; Hegg et al., 2010; Doherty et al., 2014; Wang
3 et al., 2014b). As the most important LAP (Bond et al., 2013; Doherty et al., 2010; Wang et al., 2014b;
4 Shi et al., 2020), the radiative efficiency of snowpack BC can be more than three times greater than that
5 of carbon dioxide (Flanner et al., 2007), and MD, another important snowpack LAP, is also known to
6 alter the cryospheric environment owing to its light-absorbing properties (Di Mauro et al., 2015; Painter
7 et al., 2007; Sarangi et al., 2020; Shi et al., 2021). Recently, researchers have also begun evaluating the
8 influence of biomes on global snow albedo (Hotaling et al., 2021). In contrast, however, the role of OC
9 remains poorly understood because of its complex composition and a relative dearth of OC-focused
10 research. Consequently, substantial uncertainty surrounds the origins, optical properties, and radiative
11 effects of snowpack OC.

12 The recent study has reported that the storage of OC in mountain glaciers and ice caps (~11 % of Earth's
13 land surface) could be as high as 6 petagrams (Pg), the majority of which is water-soluble organic carbon
14 (WSOC) (Hood et al., 2015; Yan et al., 2016). The substantial part of WSOC in glacier is highly
15 bioavailable and can be a source of labile organic matter for downstream ecosystems (Singer et al., 2012).
16 The physical and photochemical processes can occur within various WSOC in snow cover and glaciers,
17 and therefore have a great effect on atmospheric and glacier chemistry (Domine, 2002; Grannas et al.,
18 2007; Antony et al., 2011). Moreover, WSOC has important influences on the energy budget and
19 radiative forcing of snow cover and glaciers (Kirillova et al., 2014; Ram et al., 2010; Yan et al., 2016).
20 As the chief absorber of WSOC, water-soluble brown carbon (WS-BrC) can absorb significant measures
21 of solar radiation in the ultraviolet–visible (UV–vis) wavelengths (Murphy et al., 2008). For instance, in
22 their analysis of 21 Arctic and Antarctic snow samples, Anastasio and Robles (2007) observed that 50 %

1 of the total light absorption coefficients at wavelengths > 280 nm might be attributed to organic
2 chromophores of WSOC. Beine et al. (2011) reported that WSOC occupies almost the entire absorption
3 spectrum of the photochemically active region (300–450 nm) in surficial snow samples from Barrow,
4 Alaska. And Feng et al. (2016) observed that absorption in cryoconite samples from the central Tibetan
5 Plateau is dominated by WSOC components in the 300–350 nm range. Similarly, Yan et al. (2016)
6 measured WSOC in glacial snow from Laohugou, northern Tibetan Plateau, where they found that the
7 radiative forcing is ~ 10 % that of BC. Together, these studies indicate that WSOC plays a key role in
8 global snowpack energy absorption (Niu et al., 2018; Zhang et al., 2020). We note that recent researches
9 on cryospheric WSOC mainly focused on alpine glaciers and polar regions (Li et al., 2022; Guo et al.,
10 2022), while the extensive mid-latitude regions impacted by seasonal snowpack remain relatively
11 understudied.

12 The composition of WSOC is typically complex, and characteristics of fluorescence and absorption can
13 vary widely among the different components. Nonetheless, recent studies have tended to treat WSOC as
14 a single entity and focus on the overall impacts (Barrett and Sheesley, 2017; D'Sa et al., 2014; Niu et al.,
15 2018; Wu et al., 2019), such that the specific roles of individual components are poorly constrained. One
16 commonly used analytical method for distinguishing the components and properties of fluorescence is
17 the fluorescence excitation-emission matrices (EEMs), which has the advantage of high sensitivity and
18 small sample size (Coble, 1996; Kowalczyk et al., 2005). First applied in oceanic contexts (Coble et al.,
19 1990), EEMs have been gradually extended to lakes, fog water, rainwater (Birdwell and Valsaraj, 2010;
20 Huguet et al., 2009; McKnight et al., 2001). At present, the application of EEMs on atmospheric aerosols
21 has entered a mature stage. EEMs have been used to identify fluorescent WSOC components in aerosols
22 from polar regions or urban backgrounds, and it has been found that different structures of WSOC

1 fractions exhibit different oxidation properties, which may provide a clue to understand the chemical
2 formation or loss of organic chromophores in atmospheric aerosols (Chen et al., 2016; Fu et al., 2015).
3 Recently, this method has been gradually extended to the analysis of glacier samples and snow samples
4 (Feng et al., 2018; Guo et al., 2022; Zhou et al., 2019b). Concurrently, parallel factor analysis
5 (PARAFAC) is an effective approach for extracting from complex EEMs the individual fluorescence
6 components and their corresponding fluorescence information, thus making EEM–PARAFAC a direct
7 and viable means for exploring sources of WSOC. For example, Zhou et al., (2019b) used EEM–
8 PARAFAC to identify the multiple sources of WSOC measured in seasonal snow in northwestern China.
9 Accordingly, we have applied EEM–PARAFAC in our analysis of snow samples for this study.

10 EEM-PARAFAC can only provide plausible information about the component-specific influence of
11 WSOC on fluorescent properties, and the quantitative fractional contributions of specific components to
12 light absorption are still unknown. Recently, Chen et al. (2019a) collected atmospheric aerosol samples
13 in PM_{2.5} over Xi’an, China, and successfully attributed the dithiothreitol (DTT) activity levels to various
14 BrC components by coupling DDT and BrC datasets. A similar attribution method has been applied to
15 various research areas, including climate change, extreme weather, and atmospheric environments (Cao
16 et al., 2015; Pokrovsky, 2019; Xin et al., 2016; Zhao et al., 2019). In this study, we applied a multiple
17 linear regression method comparable to that of Chen et al. (2019a) to derive the fractional contribution
18 of each WSOC component to light absorption. Despite this method having been used elsewhere (Wu et
19 al., 2022; Wu et al., 2021), it remains a highly innovative approach to evaluating the light absorption of
20 snowpack WSOC.

21 Northeastern China supports an extensive snowpack during winter and spring. As a major industrial and
22 agricultural center, this region is also the principal source of heavy airborne pollutants that are

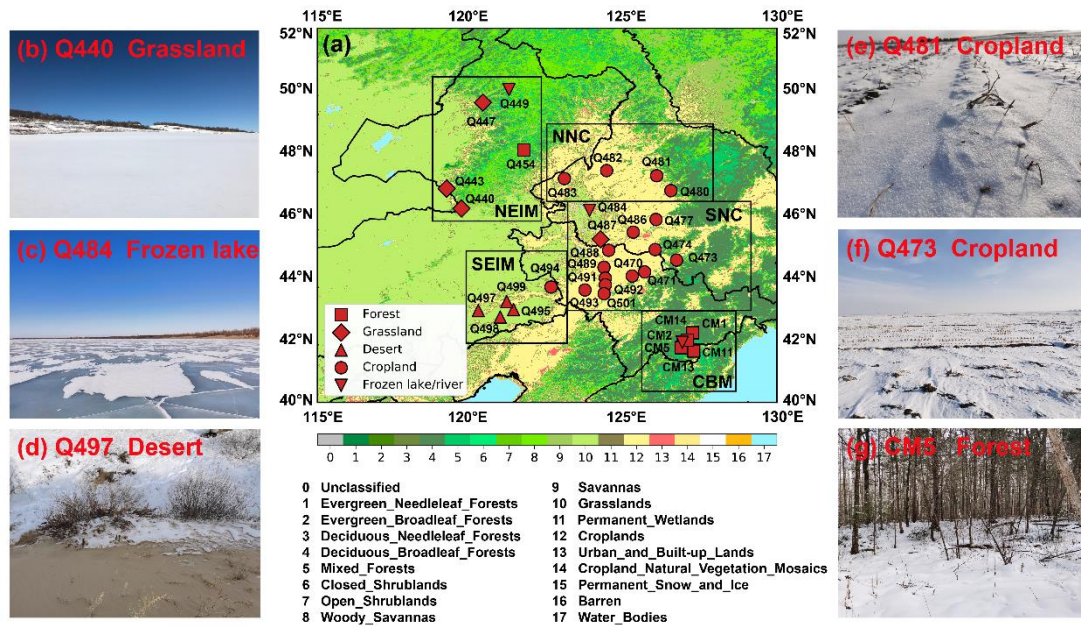
1 incorporated into seasonal snow via wet and dry deposition (Wang et al., 2017). Coupled with intensive
2 tilling of farmland, the geographical proximity of northeastern China to neighboring desert regions also
3 provides a source of soil organic matter that becomes entrained into the snowpack (Wang et al., 2013b).
4 Compared with research on BC-snow mixing ratios and their radiative impact in northeastern China
5 (Dang et al., 2017; Huang et al., 2011; Pu et al., 2019), studies of WSOC are still in their infancy. To
6 address this deficiency, we make the primary investigation of the fluorescence characteristics, absorption
7 properties, and radiative effects of WSOC in seasonal snow samples in northeastern China. Specifically,
8 we applied EEM-PARAFAC to identify the origins and fluorescence characteristics of snowpack WSOC,
9 after which we derived individual absorption contributions for each WSOC component using
10 fluorescence data, an absorption data series, and an attribution method. Finally, we estimated the
11 reduction of snow albedo and radiative forcing caused by WSOC and BC via the Spectral Albedo Model
12 for Dirty Snow (SAMDS) radiative transfer model.

13 **2 Methods**

14 **2.1 Sample collection**

15 During the months of January and December 2020 and January 2021, we collected 34 snow samples
16 from sites across northeastern China, including the eastern part of Inner Mongolia and Heilongjiang and
17 Jilin provinces. Sample numbers were set following previous campaigns (Pu et al., 2017; Wang et al.,
18 2013b, 2017), with the exception that samples from the Changbai Mountain area are numbered
19 individually. The geographical distribution of sampling sites and respective land-cover types are shown
20 in Figure 1a; our sites are characterized by five land-cover types, including forest, grassland, desert,
21 cropland, and frozen lake/river (Fig. 1b–g). On the basis of these geographical and environmental
22 classifications, we divided the sampling sites into five broad regions: southeastern Inner Mongolia (SEIM;

1 Q494–495, Q497–499), the south of northeast China (SNC; Q470–471, Q473–474, Q477, Q484, Q486–
 2 Q489, Q491–Q493, Q501), the north of northeast China (NNC; Q480–483), the Changbai Mountain area
 3 (CBM; CM1–CM2, CM5, CM11, CM13–CM14), and northeastern Inner Mongolia (NEIM; Q440, Q443,
 4 Q447, Q449, Q454).



5
 6 **Figure1: (a) Information on sampling site distributions in northeastern China, including the land cover type,**
 7 **site number, and grouping. Land cover types are derived from Collection 5.1 of the MODIS global land cover**
 8 **type dataset (MCD12Q1: <https://lpdaac.usgs.gov/products/mcd12q1v006/>) and are indicated by specific**
 9 **colors and symbols relative to sampling sites. Sampling sites are divided into the five groups defined by black**
 10 **rectangles. (b–g) Photographs depicting the typical snow and ground-cover conditions of our various sampling**
 11 **sites.**

12 Our sampling sites were chosen at random but had to be located ≥ 20 km from cities and villages and at
 13 least a kilometer upwind of roads or railroads to minimize the influence of single-point pollution sources
 14 and to ensure the broadest regional representation. Furthermore, we performed sample collection oriented
 15 toward the wind to avoid contamination from personnel. At each site, we used a sterile disposable shovel
 16 to collect 0–5 cm-thick samples of surface snow, which were subsequently stored in sterile Whirlpak
 17 (Nasco, WI, USA) bags. For snow depths < 5 cm, we determined the sampling depth according to the
 18 actual conditions to avoid inducing significant soil impurities during sampling. Snow samples were

1 melted at room temperature (25 °C) and stored in a freezer at -20 °C until analysis in the laboratory. For
2 more operational details, we refer the reader to Wang et al. (2013b).

3 **2.2 Chemical species analysis**

4 All collected snow samples were stored in a freezer at -20 °C until analyzed in the laboratory. In the lab
5 process, the samples were firstly melted at room temperature (25 °C). Then 30 mL meltwater was taken
6 for each sample with the clean disposable syringe (Jiangnan, Anhui, China) and injected into the pre-
7 baked (4h, 450 °C) glass bottle passing through 0.45 µm pore-sized polytetrafluoroethylene filters
8 (Jinteng, Tianjin, China). Finally, the concentration of WSOC was measured by the total organic carbon
9 analyzer (Aurora 1030W, OI Analytical, TX, USA), and measurement detection limits and relative
10 standard deviations were 2 µg L⁻¹ and 1 %, respectively. Additionally, a blank sample prepared with
11 ultrapure water was measured for blank correction before the sample measurement. The blank
12 concentration of WSOC is 0.35 mg L⁻¹ and the blank-corrected WSOC concentrations are provided in
13 Table S1.

14 We used 0.4 µm pore-sized polycarbonate filter membranes (Whatman, USA) to isolate BC and other
15 insoluble particles, following the protocols outlined by Wang et al. (2020), after which we employed a
16 custom-developed two-sphere integrating-sandwich (TSI) filter-based spectrophotometer to measure
17 particle absorption. Coupled with the mass of filtered meltwater, these optical measurements were then
18 converted to snowpack BC concentrations. To make these calculations, we applied a BC mass-absorption
19 coefficient (MAC) and absorption Ångström exponent (AAE) of 6.3 m² g⁻¹ (550 nm) and 1.1,
20 respectively, after Pu et al. (2017). We note that TSI provides greater accuracy and smaller overall
21 uncertainties in the quantification of seasonal snow BC than do thermo-optical carbon analysis (Wang et

1 al., 2020), and thus it has been applied widely in this type of research (Shi et al., 2020). For more detailed
2 information, we refer the reader to Wang et al. (2013b).

3 **2.3 Fluorescence and absorption measurement**

4 We obtained absorbance and fluorescence EEMs for filtered meltwater samples via synchronous
5 absorption-3D Fluorescence scanning spectrometry (Aqualog, Horiba Scientific) with the following
6 measurement parameters: fluorescence spectra excitation range = 240–800 nm in 3 nm intervals,
7 emission range = 152.25–929.92 nm in 5.04 nm (8 pixels) intervals, scanning interval = 0.3 seconds.

8 Prior to sample measurement, we analysed aliquots of filtered ultra-pure water (18.2 M ω cm, Milli-q
9 Purification System, Millipore) as analytical blanks. We normalized fluorescence intensity to that of the
10 water Raman unit (RU), which exhibits a peak excitation wavelength of 350 nm, and deducted this
11 Raman signal from all subsequent sample tests (Lawaetz and Stedmon, 2009). The inner filtration effect
12 correction is based on the absorbance-based approach (Kothawala et al., 2013), using the measured
13 absorbance at each pair of excitation and emission wavelengths across the EEMs to convert the observed
14 fluorescence intensity into the corrected fluorescence intensity. Rayleigh scattering peaks were processed
15 by interpolation algorithm in EEMscat MATLAB toolbox (Bahram et al. 2006). As fluorescence spectra
16 with wavelengths greater than 600 nm are primarily noise (Zhou et al., 2019b), they are not considered
17 further in this study. Likewise, any samples with absorption spectra of >600 nm wavelengths were
18 subtracted for the baseline correction (Chen et al., 2019b).

19 We used version 0.6.3 of the MATLAB drEEM toolbox (<http://dreem.openfluor.org/>; Murphy et al.,
20 2013) to perform PARAFAC analysis on EEMs. Comprising the consistency index, residuals, and visual
21 inspections, the 3-component model is considered more reliable and representative than are the 2–7-
22 component models (Fig. S1 in the Supplement) and passes the S4C6T3 split scheme (Fig. S2; Murphy

1 et al., 2013). The contributions of these three components to the overall fluorescence signal are expressed
 2 as relative percentages of F_{\max} in RU, and the total fluorescence volume (TFV; RU nm^2) is calculated
 3 from the EEMs (Song et al., 2019). Normalized TFV equates to NFV ($\text{RU nm}^2 (\text{mg L}^{-1})^{-1}$), TFV
 4 $c(\text{WSOC})^{-1}$), where $c(\text{WSOC})$ is the concentration of WSOC in the snow (mg L^{-1}), and represents a
 5 sample's fluorescence ability (Chen et al., 2019a).

6 We calculated three fluorescence-derived indices—the fluorescence index (FI), biological index (BIX),
 7 and humification index (HIX)—from the ratio of fluorescence intensity at specific excitation and
 8 emission wavelengths. As demonstrated by previous studies (Birdwell and Valsaraj, 2010; Huguet et al.,
 9 2009; McKnight et al., 2001), these ratios can help characterize potential sources of WSOC. Specifically,
 10 the FI is taken to represent the relative amount of DOM derived from terrestrial and microbial/algae
 11 sources (McKnight et al., 2001); high values correspond to terrestrially derived organics, and low values
 12 reflect microbial sources. The HIX describes the degree of humification of soluble organic matter
 13 (Zsolnay et al., 1999). During humification, the aromaticity of organic matter increases as microbial
 14 availability decreases, such that higher HIX values correspond to more strongly humified and/or higher
 15 aromaticity organics (principally of terrestrial origin), whereas lower values indicate autochthonous or
 16 microbial origins. As a measure of autochthonous productivity (Huguet et al., 2009), elevated BIX values
 17 are associated with increased contributions of microbial-derived fluorescent organic matter. The three
 18 indices are calculated by the following equations (Ohno, 2002; Huguet et al., 2009; McKnight et al.,
 19 2001; Feng et al., 2016):

20
$$\text{FI} = \frac{I(\text{Ex} = 370, \text{Em} = 470)}{I(\text{Ex} = 370, \text{Em} = 520)}, \quad (1)$$

21
$$\text{BIX} = \frac{I(\text{Ex} = 310, \text{Em} = 380)}{I(\text{Ex} = 310, \text{Em} = 430)}, \quad (2)$$

22
$$\text{HIX} = \frac{I(\text{Ex} = 254, \text{Em} = 435 - 480)}{I(\text{Ex} = 254, \text{Em} = 300 - 345) + I(\text{Ex} = 254, \text{Em} = 435 - 480)}, \quad (3)$$

1 where I is the fluorescence intensity, and Ex and Em represent the excitation and emission wavelengths,
2 respectively. To ensure a direct comparison with prior results, we recalculated published HIX data using
3 the same calculation methods as in our own analyses. According to a previous study, FI values of ≤ 1.4
4 correspond to terrestrial sources and values of ≥ 1.9 denote a primarily microbial origin. The values of
5 1.4–1.9 suggest a mixed origin (McKnight et al., 2001).

6 The absorption spectra of WSOC were derived from 240 to 800 nm in 3 nm intervals. The baseline shifts
7 and scattering effects of the measurement for the absorption spectra were corrected by subtracting the
8 average absorbance above 600 nm from the whole spectrum (Chen et al., 2019b). We converted sample
9 absorbance to an absorption coefficient using the following equation:

$$10 \quad a_{\text{WSOC}}(\lambda) = \ln(10) \cdot \text{Abs}(\lambda) \cdot L^{-1}, \quad (4)$$

11 where Abs is absorbance, λ is wavelength, L is the path length of the cuvette (0.01 m), and a_{WSOC} is the
12 absorption coefficient (m^{-1}).

13 Owing to the absorption characteristics of WSOC, we selected the absorption coefficient at 280 nm
14 ($a_{\text{WSOC}}(280)$) to characterize the absorption intensity of WSOC for comparison with other studies (Zhang
15 et al., 2010).

16 To investigate the wavelength dependence of WSOC absorption, we obtained the Absorption Ångström
17 exponent (AAE) via the following equation (Doherty et al., 2010; Niu et al., 2018; Wang et al., 2013b;
18 Yan et al., 2016):

$$19 \quad a_{\text{WSOC}}(\lambda) = K \cdot \lambda^{-\text{AAE}}, \quad (5)$$

20 where K is a constant related to WSOC concentration.

21 We calculated the mass absorption coefficient (MAC_λ , $\text{m}^2 \text{g}^{-1}$) of our samples using the equation (Chen
22 et al., 2019b; Yan et al., 2016):

1 $MAC_{\lambda}=a_{WSOC}(\lambda) / c(WSOC),$ (6)

2 where a_{WSOC} is the absorption coefficient derived from Equation (4) and $c(WSOC)$ ($mg L^{-1}$) is the
3 concentration of WSOC.

4 **2.4 Snow albedo modeling and radiative forcing calculations**

5 To establish the radiative effect impact of snowpack WSOC in northeastern China, we used SAMDS to
6 simulate spectral snow albedo. This model is based on asymptotic radiative transfer theory, which has
7 been verified by previous studies (Li et al., 2021b; Wang et al., 2017). As described in detail by Wang
8 et al. (2017), the model involves parameters including solar zenith angle, impurity concentrations, mass
9 absorption coefficient of impurities, and snow grain radius. Measured values include the concentration
10 of BC and absorption coefficients of WSOC. To quantify the influence of pollutants on snow albedo, we
11 assumed a semi-infinite snow layer and uniform snow grain radii of 100 μm for fresh snow and 1000 μm
12 for old snow, consistent with previous studies (Pu et al., 2021). With the solar zenith angle fixed at 60°,
13 consistent with our sampling dates and locations, we calculated the reduction ($\Delta\alpha_i$, i represents BC only,
14 WSOC only, and BC + WSOC, similarly hereinafter.) in spectral snow albedo derived from different
15 types of impurities for the UV–vis (280–400 nm) and ultraviolet–near infrared (UV–NIR; 280–1500 nm)
16 bands. Radiative forcing resulting from either BC or WSOC in snow (RF_i) was then derived by
17 multiplying the albedo reduction value by the incident solar radiation (Painter et al., 2013):

18 $RF_i=E\cdot(\alpha_{pure} - \alpha_i)=E\cdot\Delta\alpha_i,$ (7)

19 where α_{pure} is snow albedo for pure snow and E is the average daily downward shortwave solar radiation
20 flux acquired from NASA’s Clouds and the Earth’s Radiant Energy System (CERES) product “CERES
21 SYN1deg” (<https://ceres.larc.nasa.gov/products.php?product=SYN1deg>).

1 3 Results and discussion

2 3.1 Characteristics of chemical species

3 Figure 2a shows the spatial distribution of measured WSOC in seasonal snow across northeastern China.

4 Averaged across our entire study area, the mean WSOC concentration (arithmetic mean \pm standard

5 deviation) is $3.6 \pm 3.2 \mu\text{g g}^{-1}$, with a maximum of $18.0 \mu\text{g g}^{-1}$ and a minimum of $0.3 \mu\text{g g}^{-1}$. Among the

6 five regions, WSOC concentrations are highest in SNC (average $5.7 \pm 3.7 \mu\text{g g}^{-1}$), likely reflecting the

7 greater degree of agricultural and industrial activity there compared with other regions (Lu et al., 2011;

8 Wang et al., 2013b). We highlight that both agricultural and industrial sources are considered

9 anthropogenic. In contrast, our second highest measured concentrations ($3.4 \pm 1.5 \mu\text{g g}^{-1}$) are from SEIM,

10 where desertification occurs (Fang et al., 2007) and is therefore considered a natural source of WSOC.

11 For most sites, the underlying surface is desert (Fig. 1a) that was incompletely covered by seasonal snow

12 during the sampling period (Fig. 1d). Consequently, the exposure of natural sandy soils is a potentially

13 significant contributor of WSOC through aeolian erosion and dry deposition. In NNC, where both the

14 population density and agricultural intensity are lower than in SNC (Choi et al., 2020), the contribution

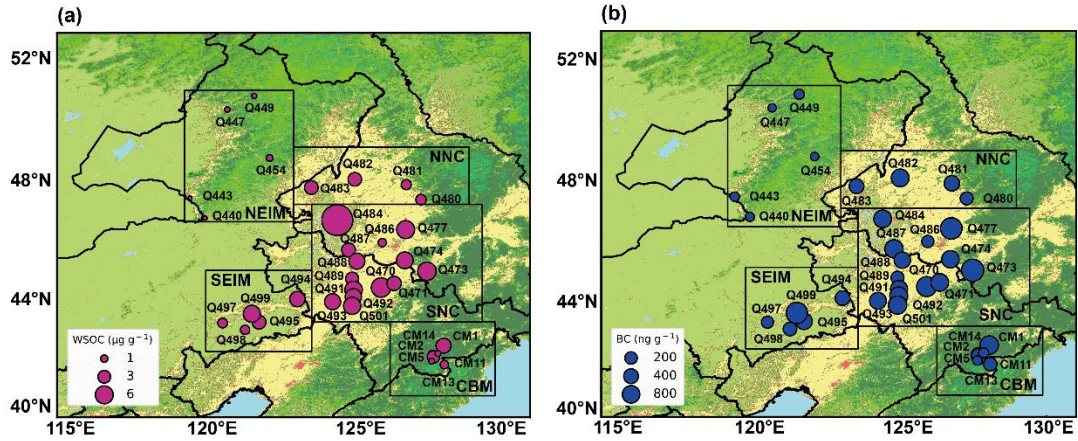
15 of anthropogenic pollution to snowpack is correspondingly lower, resulting in a moderate WSOC

16 concentration of $2.7 \pm 0.8 \mu\text{g g}^{-1}$. Meanwhile, far from intensive human activity, both CBM and NEIM

17 (Fig. 1a, b, and g) returned low WSOC concentrations (CBM: $2.0 \pm 1.3 \mu\text{g g}^{-1}$; NEIM: $0.5 \pm 0.2 \mu\text{g g}^{-1}$).

18 Nonetheless, the higher value for CBM betrays the influence of far-traveled anthropogenic pollutants

19 (Wang et al., 2015; Wu et al., 2020; Zhang et al., 2013).



1
 2 **Figure 2: Spatial distributions of concentrations of (a) WSOC and (b) BC in snow samples. Sampling sites are**
 3 **divided into the five groups defined in Figure 1. Bubble sizes are proportional to concentrations of WSOC**
 4 **and BC.**

5 In comparison with previous studies, we observed that, with the exception of NEIM, our measured
 6 WSOC concentrations are significantly higher than those reported for snow/ice from the Tibetan Plateau
 7 (TGL; $\sim 0.71\text{--}1.02 \mu\text{g g}^{-1}$; Feng et al., 2016), the Alps ($\sim 0.14\text{--}0.78 \mu\text{g g}^{-1}$; Vione et al., 2021), North
 8 America ($\sim 0.1\text{--}0.3 \mu\text{g g}^{-1}$; Fellman et al., 2015), and polar regions ($\sim 0.12\text{--}0.27 \mu\text{g g}^{-1}$; Antony et al.,
 9 2014), but comparable to values in Laohugou glacier ice from the Tibetan Plateau ($\sim 1.02\text{--}2.6 \mu\text{g g}^{-1}$;
 10 Feng et al., 2018, 2016) and seasonal snowpack in northwestern China ($0.48\text{--}7.07 \mu\text{g g}^{-1}$; Zhou et al.,
 11 2021). This finding implies that snowpack WSOC in northeastern China is contributing significantly to
 12 regional and global climate change (Domine, 2002).

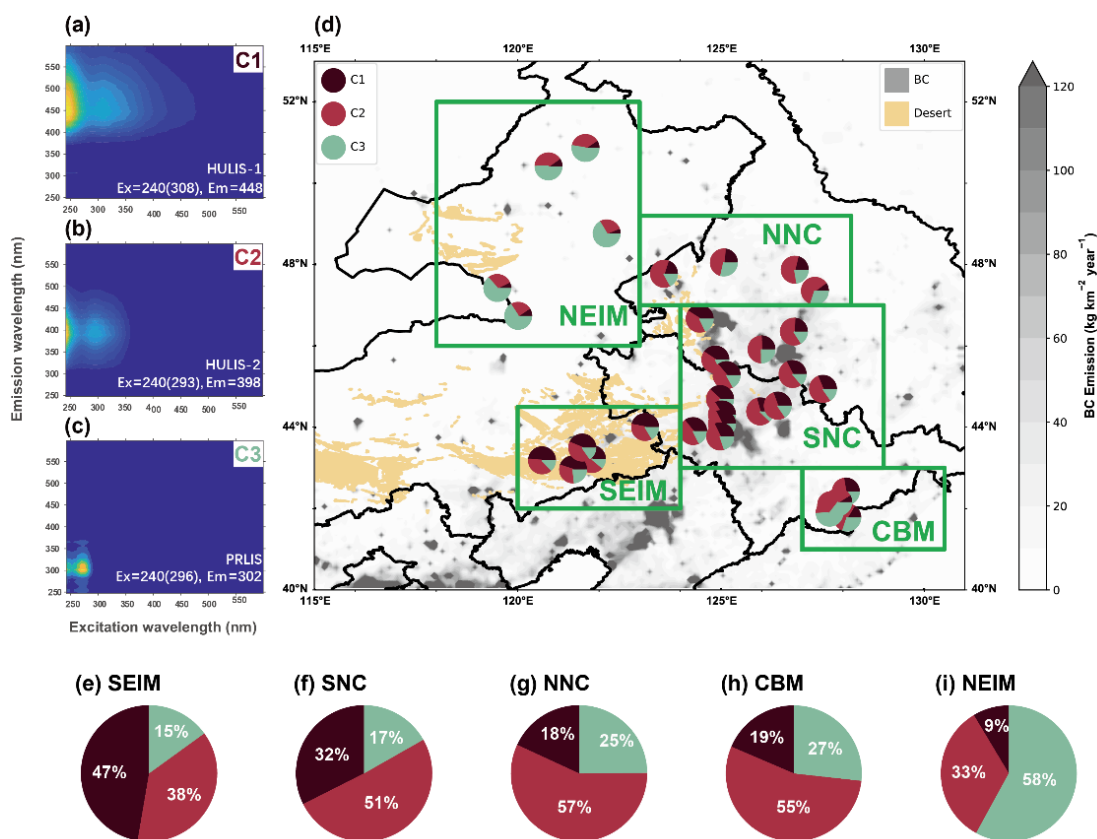
13 A similar spatial pattern is exhibited by snowpack BC (Fig. 2b). For example, of all five regions, the
 14 regional mean BC concentration is highest for SNC (mean: $923 \pm 512 \text{ ng g}^{-1}$), followed by SEIM (659
 15 $\pm 582 \text{ ng g}^{-1}$), NNC ($494 \pm 224 \text{ ng g}^{-1}$), and the CBM ($391 \pm 312 \text{ ng g}^{-1}$). BC concentrations are lowest in
 16 NEIM ($60 \pm 19 \text{ ng g}^{-1}$), in agreement with the values in remote areas reported by Doherty et al. (2010).

17 3.2 Fluorescence characteristics of WSOC

18 Three fluorescent components (C1–C3) were captured by resolving the EEMs spectra; all fluorescence
 19 information is summarized in Table S2. C1 exhibits a primary peak at $E_x = 240 \text{ nm}$, $E_m = 448 \text{ nm}$,

1 indicating a high-oxygenated humic-like substance (HULIS) found primarily in aromatic conjugated
2 macromolecules (Chen et al., 2016). The weaker secondary peak occurs at longer excitation wavelengths
3 (Ex / Em = 308 / 448 nm), implying a higher aromatic content and greater molecular weight (Coble et
4 al., 1998). Wen et al. (2021) concluded that C1 is probably derived from natural terrestrial sources, such
5 as dust and soil, as proposed originally by Stedmon et al. (2003) and Osburn et al. (2016). Accordingly,
6 we classified C1 as a terrestrial, humic-like substance, hereafter referred to as HULIS-1.

7 C2 exhibits a primary (secondary) peak at Ex = 240 (293) nm, Em = 398 nm, suggestive of
8 lower-oxygenated HULIS (Chen et al., 2016). Observed in a variety of sources, Stedmon et al. (2003)
9 reported this component in terrestrial end-member samples. Whereas, both Murphy et al. (2011) and
10 Osburn et al. (2016) have since linked C2 to anthropogenic sources, such as urban runoff and sewage.
11 Microbial activity and the degradation of phytoplankton in natural aquatic systems are also thought to
12 contribute to this component (Yamashita et al., 2008; Zhang et al., 2009). Accordingly, we classified C2
13 as humic-like substances with complex origins in terrestrial, anthropogenic, and/or microbial sources,
14 hereafter termed HULIS-2. Unlike HULIS-1 and HULIS-2, C3 is recognizable as a UVB-like protein or
15 tyrosine-like fluorescence (hereafter PRLIS) with a primary (secondary) peak at Ex = 240 (293) nm, Em
16 = 398 nm (Osburn et al., 2016; Stedmon and Markager, 2005). PRLIS reflects autochthonously labile
17 DOM produced by biological processes (Stedmon et al., 2003) and has been reported in previous studies
18 of seasonal snow (Zhou et al., 2019b).



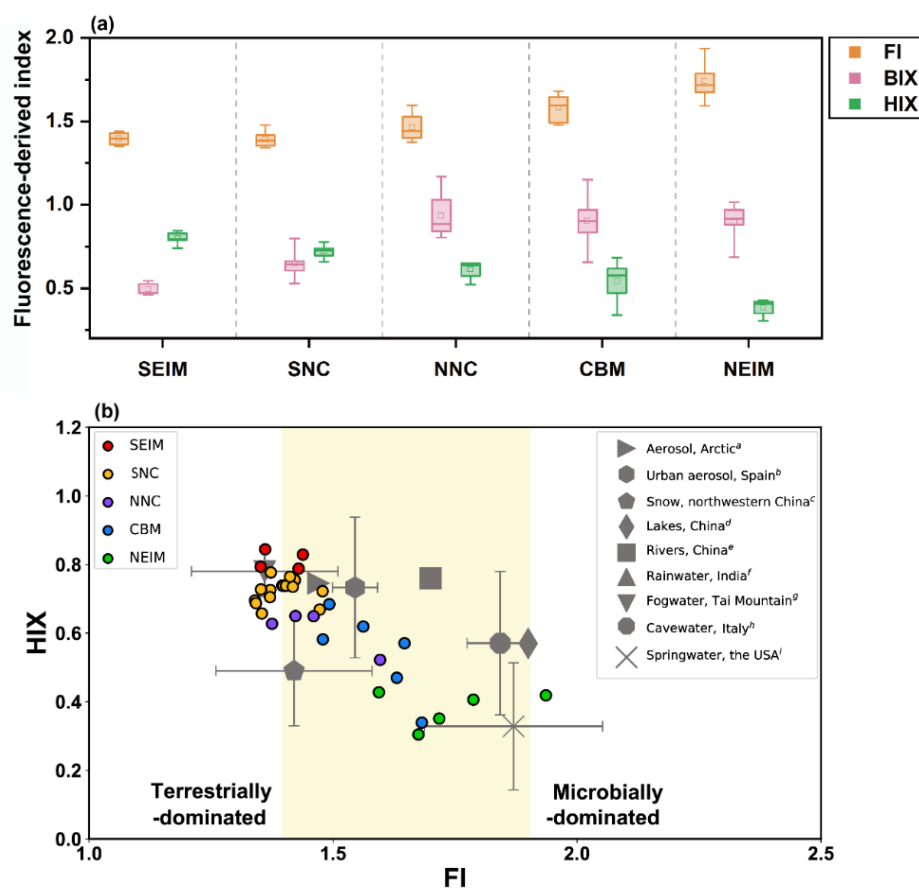
1

2 **Figure 3: (a–c) Three fluorescent components identified by PARAFAC analysis. (d) Relative contributions of**
 3 **the three components to total fluorescence at each site. HULIS-1, HULIS-2, and PRLIS are represented by**
 4 **the specific colors shown in the legend (top left corner). The distributions of BC emissions and desert areas in**
 5 **our study area are indicated by gray and light yellow, respectively, with darker gray colors indicating higher**
 6 **black carbon concentrations. (e–i) Average contributions of the three components in different groups of**
 7 **samples. BC emission data are derived from the research group at Peking University**
 8 **([http://inventory.pku.edu.cn/ home.html](http://inventory.pku.edu.cn/home.html), Wang et al., 2014a); the Chinese desert (sand) distribution dataset**
 9 **is provided by the National Tibetan Plateau Data Center ([http://poles.tpsc.ac.cn/zh-hans/data/122c9ac2-53ee-](http://poles.tpsc.ac.cn/zh-hans/data/122c9ac2-53ee-4b9a-ae87-1a980b131c9b/)**
 10 **4b9a-ae87-1a980b131c9b/; Wang et al., 2013a).**

11

12 Figure 3d depicts the spatial distribution of the relative contribution of three components to fluorescence,
 13 with the regional averages given in Figure 3e–g. In SEIM, the greatest contribution is that of HULIS-1
 14 (47 %), followed by HULIS-2 (38 %) and PRLIS (15 %), indicating that the signal is dominated by local
 15 soil/dust sources, consistent with the local environment (Figs. 2 and 3d). HULIS-2 plays a greater role
 16 in SNC, where it accounts for half of the total fluorescence signals; of the remaining half, HULIS-1 is
 17 most important. This difference in key components between SEIM and SNC illustrates the change in
 primary source of fluorescence intensity. Indeed, although HULIS-2 might be derived from any

1 combination of terrestrial, anthropogenic, and microbial sources (Osburn et al., 2016; Stedmon et al.,
2 2003; Yamashita et al., 2008; Zhang et al., 2009), human activity (e.g., agriculture, industrial emissions)
3 is most intensive in SNC. Therefore, our combined analysis suggests that anthropogenic source is the
4 main contributor to seasonal snow in SNC (Figs. 1a and 3d; Guo and Hu, 2022). The conclusion is also
5 in good agreement with previous study (Zhou et al., 2019b). As in SNC, HULIS-2 also represents
6 approximately half of the fluorescence signal in both NNC and CBM. The background environment of
7 NNC is similar to that of SNC, with dense urban cities and population. In the CBM, which is although
8 heavily forested (Fig. 1a; Guo and Hu, 2022), the long-range transport of anthropogenic pollutants is
9 responsible for the dominance of HULIS-2, as discussed in Sect. 3.1. HULIS-1 accounts for less than
10 PRLIS in both NNC and the CBM, which we posit reflects the concealment of bare soil surfaces by deep
11 snow and the importance of biological processes due to the heavy vegetation cover. PRLIS accounts
12 for >50 % of the total fluorescence signal in NEIM, followed by HULIS-2; HULIS-1 contributes
13 relatively little in this region. We attribute this pattern to both the extensive grassland and forest cover,
14 which obscures bare soil surfaces, and the distance from anthropogenic pollution. These together serve
15 to amplify the importance of biological processes (Zhou et al., 2019a). Taken as a whole, the respective
16 contributions of HULIS-1, HULIS-2, and PRLIS to the fluorescence signals in our study area are ~30 %,
17 ~50 %, and ~20 %. We note that these findings correspond well with the background environmental
18 conditions.



1
 2 **Figure 4: (a) Variations in fluorescence-derived indices among the five groups. Boxes denote the 25th and 75th**
 3 **quantiles, and horizontal lines represent median values. Averages are shown as small boxes, the whiskers**
 4 **denoting maximum and minimum data. (b) Comparison plots of HIX versus FI for the seasonal snow surface**
 5 **samples (colored dots) from northeastern China, together with the average and standard deviation of different**
 6 **types of WSOC (grey markers) adapted from: Arctic aerosols (^a Fu et al., 2015), Spanish urban aerosols (^b**
 7 **Mladenov et al., 2011), seasonal snowpack in northwestern China (^c Zhou et al., 2019b), Chinese lakes and**
 8 **rivers (^{d, e} Zhou et al., 2017), rainwater from Rameswaram, India (^f Salve et al., 2012), fog water from Tai**
 9 **Mountain, China (^g Birdwell and Valsaraj, 2010), cave water from Frasassi Caves, Italy (^h Birdwell and Engel,**
 10 **2010), and spring water in the USA (ⁱ Birdwell and Engel, 2010). Shaded areas represent mixed WSOC**
 11 **signatures.**

12 The FI, BIX, and HIX indices reveal spatial variability in fluorescence characteristics and thus permit
 13 the tracing of potential sources. Regionally averaged FI, BIX, and HIX values are depicted in Figure 4a.

14 Our results show that, in general, FI varies in the range of 1.34–1.94 (mean = 1.49), BIX between 0.46
 15 and 1.17 (mean = 0.74), and HIX between 0.30 and 0.84 (mean = 0.64). By comparison, reported mean
 16 FI, BIX, and HIX values for seasonal snow in Xinjiang (northwestern China) are 1.42, 0.76, and 0.55,
 17 respectively (Zhou et al., 2019b), suggesting that the impact of humification and WSOC aromaticity are

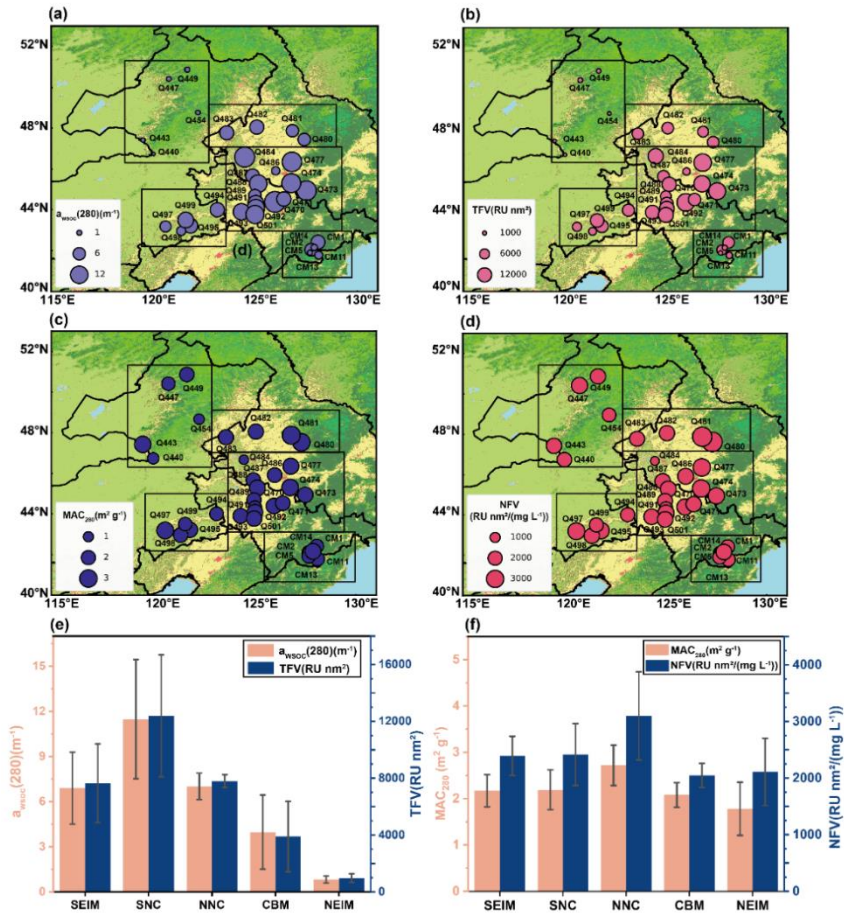
1 slightly higher in our study area than in Xinjiang. This outcome implies a relatively strong terrigenous
2 signal and correspondingly weaker biogenic signal in the seasonal snowpack of northeastern China.
3 Regionally, SEIM exhibits the lowest FI (mean = 1.40) and BIX (mean = 0.49) values but the largest
4 HIX value (mean = 0.80), further confirming the strong influence of highly aromatic, terrestrially derived
5 WSOC in this region relative to the others. In contrast, NEIM returns the highest FI (mean = 1.74) and
6 BIX (mean = 0.89) values, but the lowest HIX value (mean = 0.38), indicating the dominance of low-
7 aromatic WSOC of microbial origin. Intriguingly, our results reveal that FI and BIX rise generally with
8 decreasing (increasing) fractional contributions of HULIS-1 (PRLIS), whereas HIX exhibits a similar
9 but contrasting pattern. Together, the comprehensive dataset described above verifies the regional
10 variability in the terrestrial contributions to WSOC, in which SEIM > SNC > NNC > CBM > NEIM; this
11 pattern is reversed for microbially sourced WSOC.

12 Figure 4b illustrates HIX versus FI as a scatterplot, compared with published data for different sample
13 types; the shaded area depicts the region in which the FI value is >1.4 but <1.9. In general, FI exhibits a
14 rising trend with declining HIX across northeastern China. For both SEIM and SNC, FI occupies a
15 narrow range centered on 1.4, indicating either a predominantly terrestrial or mixed origin. We note that
16 these results are comparable to those of fog water from the Tai Mountain, Arctic atmospheric aerosols,
17 and seasonal snow in northwestern China (Birdwell and Valsaraj, 2010; Fu et al., 2015; Zhou et al.,
18 2019b). Further, we highlight that HIX values are marginally higher in SEIM than elsewhere, suggesting
19 a stronger influence from highly humified WSOC that probably reflects the extensive deserts and
20 exposed earth in this region. FI values for NNC and the CBM fall within the range of 1.4–1.7 and thus
21 reflect a mixed origin, in line with previous data from urban aerosols in Spain and Chinese river water
22 samples (Mladenov et al., 2011, Zhou et al., 2017). When combined, FI and HIX values for NNC and

1 CBM snowpack indicate that WSOC in these regions bears a stronger terrestrial signature than do water
2 samples from Chinese lakes and Italian caves (Birdwell and Engel, 2010; Zhou et al., 2017). Finally, FI
3 values for NEIM fall within a range of 1.6–2.0, comparable to values from spring water in the USA
4 (Birdwell and Engel, 2010), thus implying a predominantly microbial or mixed origin.

5 **3.3 Comparisons of fluorescence and absorption characteristics**

6 Figure 5a describes the spatial distribution of $a_{\text{WSOC}}(280)$ as WSOC absorption in the snowpack of
7 northeastern China; Figure 5b depicts TFV as a measure of the spatial distribution of absolute WSOC
8 fluorescence intensity for comparison. In general, TFV and $a_{\text{WSOC}}(280)$ both exhibit large spatial
9 variability in the range of 690–18600 $\text{RU}\cdot\text{nm}^2$ and 0.42–16.98 m^{-1} , respectively. Regional mean values
10 are $7700 \pm 2800 \text{RU}\cdot\text{nm}^2$ (TFV) and $6.90 \pm 2.39 \text{m}^{-1}$ ($a_{\text{WSOC}}(280)$) for SEIM, $12400 \pm 4300 \text{RU}\cdot\text{nm}^2$
11 (TFV) and $11.48 \pm 3.96 \text{m}^{-1}$ ($a_{\text{WSOC}}(280)$) for SNC, $7800 \pm 500 \text{RU}\cdot\text{nm}^2$ (TFV) and $7.02 \pm 0.88 \text{m}^{-1}$
12 ($a_{\text{WSOC}}(280)$) for NNC, $3900 \pm 2500 \text{RU}\cdot\text{nm}^2$ (TFV) and $3.97 \pm 2.46 \text{m}^{-1}$ ($a_{\text{WSOC}}(280)$) for the CBM,
13 and $1000 \pm 300 \text{RU}\cdot\text{nm}^2$ (TFV) and $0.83 \pm 0.23 \text{m}^{-1}$ ($a_{\text{WSOC}}(280)$) for NEIM. We note that both
14 distributions are consistent in space (Fig. 5e), with the highest concentrations in SNC and the lowest in
15 NEIM. Moreover, the $a_{\text{WSOC}}(280)$ value for SNC is an order of magnitude larger than that for NEIM,
16 implying that the impact of WSOC on snow albedo at UV wavelengths is significant in SNC but less
17 notable in NEIM in general (see Sect. 3.5). Previous work has reported a similarly broad range of
18 snowpack $a_{\text{WSOC}}(280)$ (0.15–10.57 m^{-1}) in northwestern China (Zhou et al., 2019b).



1

2 **Figure 5: Spatial distribution of (a) $a_{wSOC(280)}$ (m⁻¹), (b) TFV (RU nm²), (c) MAC₂₈₀ (m² g⁻¹) and (d) NFV**
 3 **(RU nm² (mg L⁻¹)⁻¹). Regional averages for (e) $a_{wSOC(280)}$, TFV, (f) MAC₂₈₀ and NFV for the five groups.**
 4 **Error bars in (e) and (f) represent the standard deviations of $a_{wSOC(280)}$, MAC₂₈₀, TFV, and NFV for the five**
 5 **groups, respectively.**

6

Two additional fluorescence and absorption capacity indices, identified as NFV and MAC₂₈₀, are proven

7

tools for revealing WSOC's fluorescence and absorption characteristics and they are related to chemical

8

composition, structure, and source (Chen et al., 2019a). For our study area as a whole, mean NFV and

9

MAC₂₈₀ values are 2412 ± 374 RU nm² (mg L⁻¹)⁻¹ and 2.2 ± 0.5 m² g⁻¹, respectively. Both indices exhibit

10

a narrow range, with regional means ranging from 2100 ± 600 to 3100 ± 800 RU nm² (mg L⁻¹)⁻¹ and

11

from 1.8 ± 0.6 to 2.7 ± 0.4 m² g⁻¹, respectively, in contrast to the broad inter-regional disparities in TFV

12

and $a_{wSOC(280)}$. Moreover, the spatial patterns of NFV and MAC₂₈₀ are similar, with the highest values

13

in NNC. We speculate that this result reflects the comparatively high low-oxygenated HULIS-2 fraction

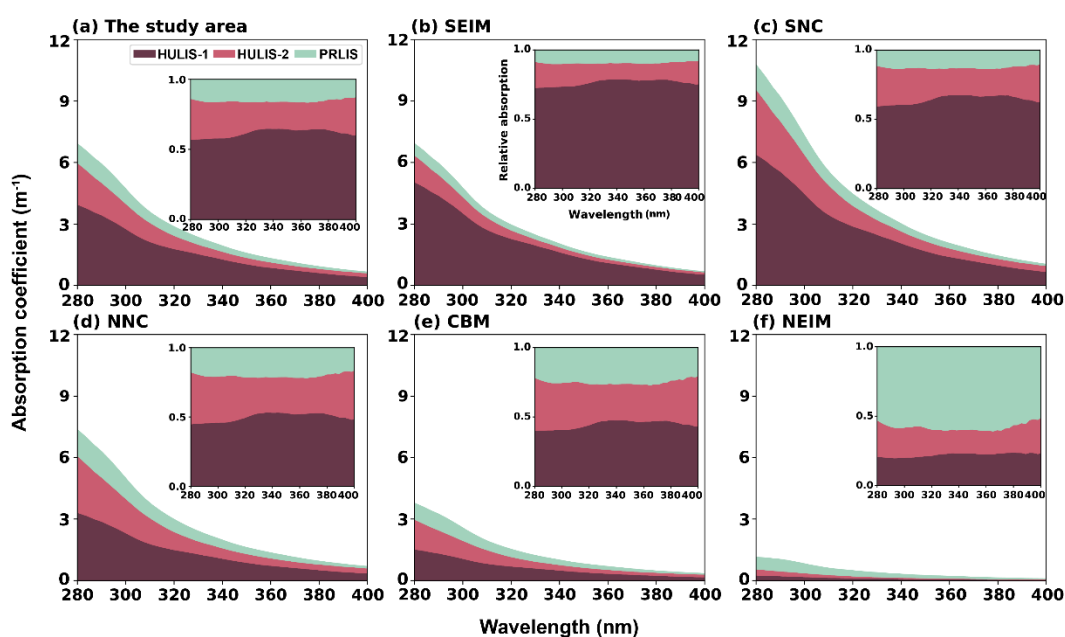
1 measured in the NNC samples (Fig. 3g), as the lower-oxygenated BrC (e.g., HULIS-2) has a higher
2 absorption capacity (Browne et al., 2019).

3 Scatterplots for $a_{\text{WSOC}}(280)$ with TFV, $F_{\text{max}}(\text{HULIS-1})$, $F_{\text{max}}(\text{HULIS-2})$, and $F_{\text{max}}(\text{PRLIS})$ are provided
4 in Figure S4 to further demonstrate the close relationship between fluorescence and the absorption
5 characteristics of WSOC in our snow samples. As samples Q480, Q484, and Q477 deviate considerably
6 from the respective confidence intervals, we did not include them in our analyses. Surprisingly, we found
7 that TFV is closely correlated to $a_{\text{WSOC}}(280)$, with $P < 0.001$ and all datapoints located close to the line
8 of best fit, indicating that the three components (HULIS-1, HULIS-2, PRLIS) contributing to the total
9 fluorescence are also responsible for the majority of absorption. For each component, our data show that
10 $F_{\text{max}}(\text{HULIS-1})$ is most closely correlated with $a_{\text{WSOC}}(280)$, followed by $F_{\text{max}}(\text{HULIS-2})$. The correlation
11 between $F_{\text{max}}(\text{PRLIS})$ and $a_{\text{WSOC}}(280)$ is the poorest, yet it is still significant ($P < 0.001$). Together, our
12 results imply that HULIS-1 is probably the greatest contributor to light absorption, with PRLIS being the
13 least important.

14 **3.4 Fractional contributions of different WSOC components to light absorption**

15 In this study, we applied a multiple linear regression method comparable to that of Chen et al. (2019a)
16 to derive the fractional contribution of each WSOC component to light absorption. Table S3 lists the
17 statistical results of the fitted light absorption coefficient, based on the F_{max} data for three fluorescent
18 components of EEM analysis. As the fitted results can explain ~94 %–99 % of the variance in measured
19 light absorption within the 280–400 nm range, we conclude that the fusion of multiple fluorescent
20 components is an effective means of describing most of the spatial features of WSOC light absorption
21 throughout northeastern China. Accordingly, the wavelength-dependent fractional contributions of each
22 component of light absorption in this band (280–400 nm) are reported in Figure 6. For our entire study

1 area, light absorption is dominated by high-oxygenated HULIS-1, which accounts for ~56 %–65 % of
 2 the contribution across UV wavelengths. Further, we observed that the HULIS-1 contribution rises
 3 slightly from 280 to ~340 nm, after which there is a decreasing trend as wavelength increases. In contrast,
 4 HULIS-2 exhibits a valley-type pattern in fractional contribution between 280 and 400 nm and is
 5 responsible for ~19 %–30 % of all light absorption.

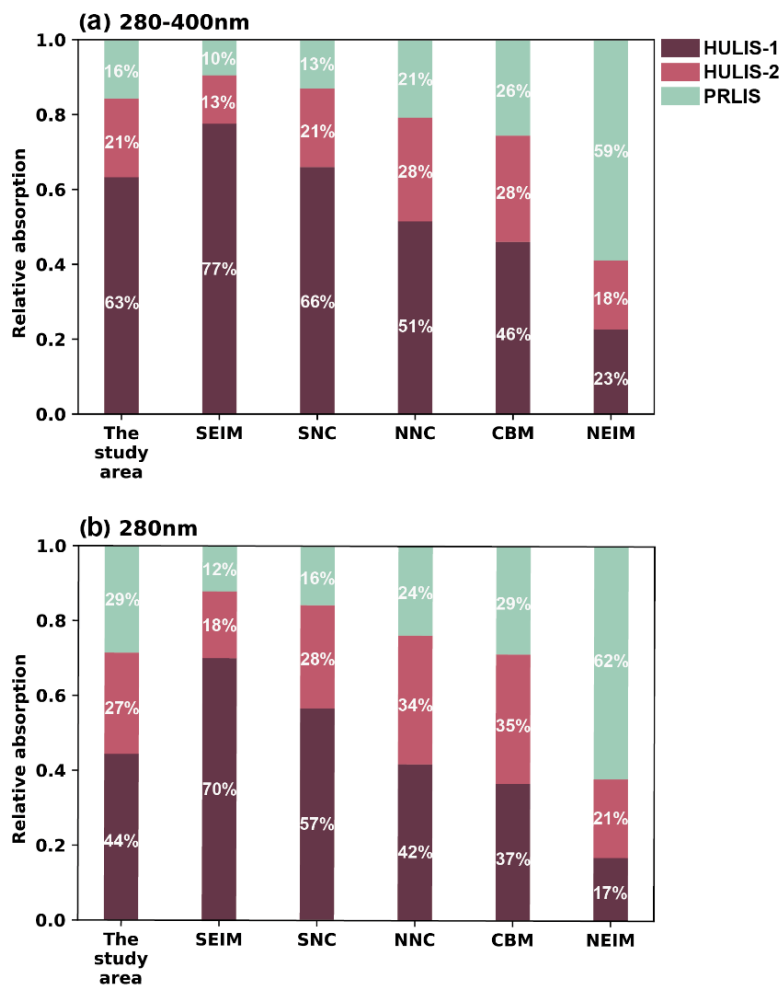


6
 7 **Figure 6: Relative contributions of the three components to the total absorption of samples in (a) the whole**
 8 **study area and (b–f) each of the five groups.**

9 PRLIS contributes the least (~12 %–17 %) to light absorption and exhibits a similar wavelength-
 10 dependent pattern to HULIS-1. These results are consistent with the qualitatively comparative analysis
 11 described in Sect. 3.3. Previous studies have also highlighted this dominance of high-oxygenated
 12 compounds in WSOC light absorption, based on samples impacted by naturally and anthropogenically
 13 derived soils (Zhou et al., 2022). Conversely, the total absorption coefficient of WSOC decreases with
 14 increasing wavelength between 280 and 400 nm, in accord with previous studies (Andreae and Gelencser,
 15 2006; Chakrabarty et al., 2010; Gustafsson et al., 2009; Wu et al., 2019). The AAE lies primarily between
 16 5.0 and 8.0 (mean = 6.6) in the range of 280–400 nm, which is in agreement with results from snow

1 collected from the Arctic, the northern Tibetan Plateau, and northwestern China (Voisin et al., 2012; Yan
2 et al., 2016; Zhou et al., 2021).

3 For each component, the wavelength-dependent variability in light absorption is similar among all five
4 regions, although the magnitude of each contribution varies from region to region. Moreover, compared
5 with the spectral results, we found that the solar-radiation-weighted broadband light absorption was a
6 more meaningful parameter for researchers studying climate change and atmospheric radiation.
7 Therefore, the broadband results in Figure 7a for 280–400 nm absorption contributions—HULIS-1
8 (62 %), HULIS-2 (21 %), and PRLIS (17 %)—are average values for the whole study area. On a regional
9 scale, the HULIS-1 contribution to light absorption (280–400 nm) follows the spatial pattern SEIM >
10 SNC > NNC > CBM > NEIM. We note that HULIS-1 dominates light absorption in SEIM, SNC, and
11 NNC but has a minor impact in NEIM compared with the other two components. In contrast, the impact
12 of HULIS-2 varies only slightly among the five regions, with the greatest contributions in NNC and
13 CMB, and the lowest in NEIM. The contribution of PRLIS is essentially opposite that of HULIS-1, being
14 dominant in NEIM but of relatively minor important elsewhere. As shown in Figure 7b, light absorption
15 contributions at 280 nm are consistent with the broadband results (Fig. 7a) in terms of the regional pattern,
16 although specific values differ because of the different wavelength-dependent properties of light
17 absorption for the three WSOC components.



1

2 **Figure 7: Regional averages for the relative contributions of the three fluorescent components to light**
 3 **absorption at wavelengths of (a) 280–400 nm and (b) 280 nm.**

4 We find it noteworthy that, for each component, the overall regional pattern of its contribution to light

5 absorption aligns with its impact on fluorescence signals, thereby confirming the viability of the

6 attribution analysis employed in our study. Nonetheless, we observed that the magnitude of each

7 component’s contribution varies relative to its respective fluorescence signal. For instance, HULIS-1

8 returns a greater contribution to light absorption than its fluorescence signal, in contrast to HULIS-2.

9 One plausible explanation for this discrepancy is that the fluorescence quantum yields (AQYs), which

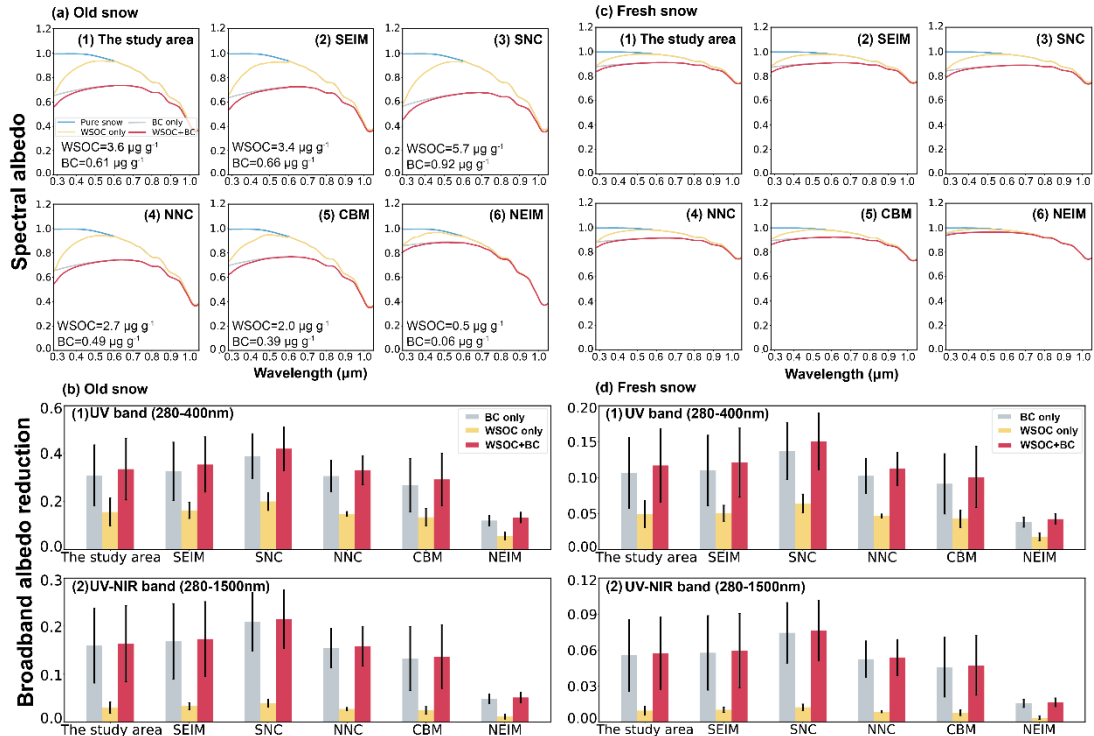
10 are essentially the ratio of fluorescence intensity versus absorption intensity, are different for each

11 component. Indeed, in their comprehensive field-based study of BrC fluorescence and absorption

1 properties in northern China, Wen et al. (2021) reported that the AQYs of WSOC decrease with
2 increasing HIX, meaning that components with higher HIX values. Such as HULIS-1, have lower AQYs
3 than does HULIS-2. Thus, the contribution of HULIS-1 to the fluorescence signals will be smaller than
4 its contribution to light absorption, and vice versa for HULIS-2.

5 **3.5 Albedo reduction and radiative forcing attributed to snowpack WSOC**

6 The strong light absorption of WSOC in UV bands has important ramifications for snow albedo and
7 radiative forcing throughout northeastern China. However, owing to the chemical and optical complexity
8 of WSOC components, quantitative estimates for snowpack light absorption remain poorly understood.
9 For example, although prior work in northeastern China has focused on BC (Wang et al., 2013b) and
10 other water-insoluble light-absorbing particles (Wang et al., 2017; Zhao et al., 2014) via field
11 measurements, model simulations, and satellite remote sensing (Pu et al., 2019), the specific impacts of
12 WSOC have not been studied. Consequently, ours is the first study to report on the impact of WSOC on
13 snow albedo and radiative forcing in northeastern China and to compare these data with BC results to
14 highlight the non-negligible role of WSOC.



1

2 **Figure 8: (a) and (b): Simulated snow spectral albedo and broadband albedo reductions—under various**
 3 **contamination scenarios and for different regions—for old snow (radius = 1000 μm). (c), (d) Simulated snow**
 4 **spectral albedo and broadband albedo reductions—under various contamination scenarios and for different**
 5 **regions—for fresh snow (radius = 100 μm). Colors represent the different types of snow (pure snow, BC- or**
 6 **WSOC-contaminated snow, and snow polluted by both WSOC and BC).**

7 Figure 8 shows the regional-mean spectral snow albedo as well as the reduction in albedo due to WSOC,

8 BC, and WSOC + BC. We assume a snow radius of 100 μm for fresh snow and 1000 μm for old snow.

9 Our findings reveal that WSOC induces a marked decline in albedo within the UV and short-wave VIS

10 bands, with the magnitude of albedo reduction growing rapidly as wavelength shrinks owing to the large

11 AAE value of WSOC. In comparison, BC induces a widespread albedo reduction spanning the UV to

12 NIR bands, and wavelength-dependent variations are significantly smaller than those of WSOC. For VIS

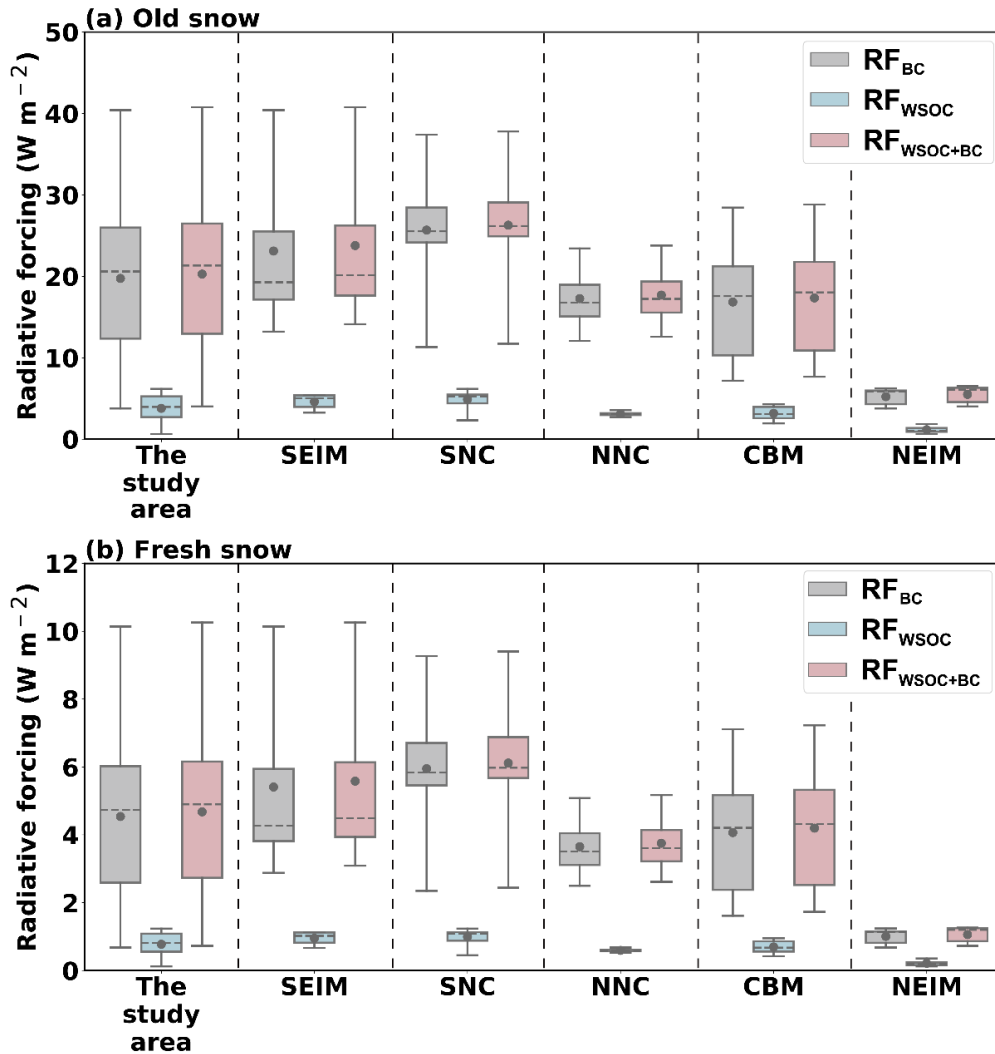
13 and NIR, the reduction in albedo is dominated by BC, whereas the impacts of WSOC and BC are

14 comparable in UV wavelengths, a pattern that is consistent with the results of studies of atmospheric

15 aerosols (Shamjad et al., 2016). We note that these characteristics persist throughout northeastern China

16 despite regional variability in environmental conditions and snowpack types (old vs. fresh snow).

1 For broadband wavelengths, our results indicate that the WSOC-induced (mean = 3.6 $\mu\text{g g}^{-1}$) albedo
2 reduction for 280–400 nm wavelength in old (fresh) snow is 0.16 (0.05) across the whole study area,
3 which corresponds to approximately 50.3 % (46.3 %) the impact of BC (mean = 0.6 $\mu\text{g g}^{-1}$). Regionally,
4 the greatest decline in albedo occurred in SNC, where a mean WSOC of 5.7 $\mu\text{g g}^{-1}$ resulted in a reduction
5 of 0.20 (0.06) in the 280–400 nm range for old (fresh) snow. In contrast, the smallest decline in albedo
6 was observed in NEIM, with reductions of 0.06 (0.02) resulting from an average WSOC concentration
7 of 0.5 $\mu\text{g g}^{-1}$. Compared with the UV bands, a WSOC-induced albedo reduction of 0.03 (0.009) over the
8 UV–NIR range (280–1500 nm) accounts for only ~18.8 % (16.7 %) of that due to BC in our study area.
9 The regional mean for old (fresh) snow falls in the range of 0.01–0.04 (0.003–0.012), with the highest
10 (lowest) values occurring in SNC (NEIM). However, we observed the highest ratio of WSOC- to BC-
11 induced albedo reduction in NEIM. Together, these results indicate that WSOC plays a potentially
12 important role in altering UV snow albedo in NEIM, despite its relatively low concentrations in the
13 regional snowpack.



1

2 **Figure 9: Radiative forcing due to different pollutants in (a) old or (b) fresh snow. Gray, blue, and red indicate**
 3 **the radiative forcing of BC, WSOC, and BC + WSOC, respectively.**

4 Radiative forcing is an important index that directly reflects the impact of snowpack WSOC on the

5 regional radiation balance and climate (Beres et al., 2020). Previous studies have tended to focus on

6 calculating instantaneous radiative forcing values; however, in reality, time-averaged results are more

7 valuable for climate research. Here, we present data on the daily mean radiative forcing due to WSOC,

8 BC, and WSOC + BC (Fig. 9). In general, for northeastern China we found the mean radiative forcing

9 of WSOC in old (fresh) snow to be 3.78 (0.77) W m⁻², with regional mean values varying from 1.15

10 (0.21) to 4.88 (1.0) W m⁻². Zhou et al. (2021) reported daily mean radiative forcing by regional WSOC

1 (0.6–7.1 $\mu\text{g g}^{-1}$) of between ~ 0.04 and $\sim 0.59 \text{ W m}^{-2}$ for northwestern China, which is comparable to our
2 values in fresh snow. Furthermore, the ratio of WSOC-driven to BC-driven radiative forcing varies
3 within the range of 10.3 %–32.0 % (9.8 %–30.8 %) for old (fresh) snow, which is consistent with the
4 results of our calculated albedo reductions. These results confirm that the role of WSOC must not be
5 ignored in discussions about radiative balance in northeastern China. Similarly, the sizeable impact of
6 WSOC on the absorption of UV radiation has the potential to influence biogeochemistry (Helms et al.,
7 2013; Seekell et al., 2015), snow photochemical processes (e.g., photolysis of nitrate (NO_3^-) and nitrite
8 (NO_2^-) in snow, in addition to the release of NO_x ($\text{NO} + \text{NO}_2$ and HONO). Snow photochemistry is
9 beyond the scope of this study, however, the high concentrations of WSOC and nitrate (not shown)
10 pollution in northeastern China make this a logical next step for research in this field.

11 **4 Conclusions and atmospheric implications**

12 During 2020 and 2021, we collected 34 surface samples of seasonal snow from sites throughout
13 northeastern China to investigate the fluorescence characteristics, optical properties, and radiative effects
14 of snowpack WSOC. With an average concentration of WSOC of $3.6 \pm 3.2 \mu\text{g g}^{-1}$, our results returned
15 regional mean values of $3.4 \pm 1.5 \mu\text{g g}^{-1}$ (SEIM), $5.7 \pm 3.7 \mu\text{g g}^{-1}$ (SNC), $2.7 \pm 0.8 \mu\text{g g}^{-1}$ (NNC), $2.0 \pm$
16 $1.3 \mu\text{g g}^{-1}$ (CBM), and $0.5 \pm 0.2 \mu\text{g g}^{-1}$ (NEIM), indicating a considerable degree of regional variability
17 of WSOC mass loadings. Measured values of WSOC fluorescence intensity (690–18600 RU nm^2) and
18 light absorption ($0.4\text{--}17.0 \text{ m}^{-1}$) are also highly variable.

19 Moreover, we also used EEMs and PARAFAC to identify three fluorescence WSOC components
20 prevalent in northeastern China, and analyzed their regional differences. In SEIM, which is characterized
21 by desert and bare soil surfaces, the signal of high-oxygenated and terrigenous HULIS-1 is dominant
22 (47 %). The high degree of humification and minimal bioavailability of WSOC, indicating that snowpack

1 WSOC originates primarily from soil sources. In contrast, the autochthonous PRLIS signal (58 %)
2 dominates in remote and clean NEIM. Low-oxygenated and anthropogenic HULIS-2 dominates the
3 densely populated and intensively farmed SNC (51 %) and NNC (57 %) regions, leading us to conclude
4 that the snowpack WSOC in SNC and NNC are influenced more by anthropogenic source. In CBM of
5 forest environment, the impact of long-distance transport of pollutants is greater than that of the
6 background environment. The above conclusions are also verified by fluorescence-derived indices.
7 We employed multiple regression analysis to estimate the fractional contributions of different WSOC
8 components to snowpack light absorption. Throughout our study area, HULIS-1 tends to be the greatest
9 contributor (~56 %–65 %) over the 280–400 nm range, followed by HULIS-2 (~19 %–30 %) and PRLIS
10 (~12 %–17 %). In contrast to its primary role in fluorescence, the contribution of HULIS-2 to light
11 absorption is relatively low across all regions, potentially reflecting the variable molecular structure of
12 different components. Finally, we highlighted that the average RF due to WSOC in old (fresh) snow in
13 northeastern China is 3.8 (0.8) W m^{-2} , which is equal to 19 % (17 %) of the BC-induced radiative forcing.
14 Therefore, we demonstrated the important impacts of WSOC on the snow energy budget and potentially
15 on triggering snow photochemistry. We indicate that our study could contribute to the understanding
16 of carbon cycling processes, regional air quality, hydrological processes, and climate change in the earth
17 systems. For example, the abundant WSOC concentrations measured in this study implied the
18 significant carbon input from the atmosphere to the snowpack through wet or dry depositions in
19 northeastern China. While the complex chemical compositions of snowpack WSOC could further
20 influence the carbon balance of the snow environment by affecting microbial activities (Stedmon et al.,
21 2007). The strong absorption properties of WSOC in the UV–Vis band also implied its important role in
22 initiating snow photochemistry (McNeill et al., 2012). It will change the composition of organic

1 compounds in the snow in turn (Grannas et al., 2007), and affect the surrounding air quality by releasing
2 oxidizing gas like NO_x into the atmosphere (Zatko et al., 2013). Moreover, the non-negligible influence
3 of WSOC on the snow albedo and radiative effect indicated that it could not only accelerate snow melting,
4 change the periods and mass of water and carbon exchange between snowpack and underlying soils or
5 vegetation (Meyer and Wania, 2008), but also potentially affect regional climate through changing the
6 surface radiative balance (Beres et al., 2020).

7

1 *Data availability.* Data presented and used throughout this study can be accessed through the
2 following data repository: <https://doi.org/10.5281/zenodo.6541956>.

3 *Supplement.* The supplement related to this article is available online at:

4 *Author contributions.* XN and WP designed the study and wrote the first draft with contributions
5 from all coauthors. XN designed and conducted the lab experiments with the assistance of YZ and
6 HW. XN processed the data with the assistance of DW and TS. XN, WP, YC, YX, TS designed
7 and conducted the field campaign. XW supervised this study. All co-authors commented on the
8 paper and improved it.

9 *Competing interests.* The authors declare that they have no conflict of interest.

10 *Acknowledgements.* The Lanzhou University group acknowledges support from the National
11 Science Fund for Distinguished Young Scholars and the National Natural Science Foundation of
12 China.

13 *Financial support.* This research was supported by the National Science Fund for Distinguished
14 Young Scholars (42025102), the National Natural Science Foundation of China (42075061 and
15 41975157), and the Lanzhou City's scientific research funding subsidy to Lanzhou University.
16

1 **References**

- 2 Anastasio, C. and Robles, T.: Light absorption by soluble chemical species in Arctic and Antarctic snow,
3 J. Geophys. Res., 112, D24304, <https://doi.org/10/dt7c54>, 2007.
- 4 Andreae, M. O. and Gelencser, A.: Black carbon or brown carbon? The nature of light-absorbing
5 carbonaceous aerosols, Atmos. Chem. Phys., 6, 3131-3148, <https://doi.org/10/fd772v>, 2006.
- 6 Antony, R., Grannas, A. M., Willoughby, A. S., Sleighter, R. L., Thamban, M., and Hatcher, P. G.: Origin
7 and Sources of Dissolved Organic Matter in Snow on the East Antarctic Ice Sheet, Environ. Sci.
8 Technol., 48, 6151–6159, <https://doi.org/10.1021/es405246a>, 2014.
- 9 Bahram, M., Bro, R., Stedmon, C., and Afkhami, A.: Handling of Rayleigh and Raman scatter for
10 PARAFAC modeling of fluorescence data using interpolation, J. Chemom., 20, 99–105,
11 <https://doi.org/10.1002/cem.978>, 2006.
- 12 Barnett, T. P., Pierce, D. W., Hidalgo, H. G., Bonfils, C., Santer, B. D., Das, T., Bala, G., Wood, A. W.,
13 Nozawa, T., Mirin, A. A., Cayan, D. R., and Dettinger, M. D.: Human-Induced Changes in the
14 Hydrology of the Western United States, Science, 319, 1080–1083,
15 <https://doi.org/10.1126/science.1152538>, 2008.
- 16 Barrett, T. E. and Sheesley, R. J.: Year-round optical properties and source characterization of Arctic
17 organic carbon aerosols on the North Slope Alaska, J. Geophys. Res.-Atmos., 122, 9319–9331,
18 <https://doi.org/10.1002/2016JD026194>, 2017.
- 19 Battin, T. J., Luysaert, S., Kaplan, L. A., Aufdenkampe, A. K., Richter, A., and Tranvik, L. J.: The
20 boundless carbon cycle, Nature Geosci., 2, 598–600, <https://doi.org/10.1038/ngeo618>, 2009.
- 21 Beine, H., Anastasio, C., Esposito, G., Patten, K., Wilkening, E., Domine, F., Voisin, D., Barret, M.,
22 Houdier, S., and Hall, S.: Soluble, light-absorbing species in snow at Barrow, Alaska, J. Geophys. Res.,

1 116, D00R05, <https://doi.org/10.1029/2011JD016181>, 2011.

2 Beniston, M., Farinotti, D., Stoffel, M., Andreassen, L. M., Coppola, E., Eckert, N., Fantini, A., Giacona,
3 F., Hauck, C., Huss, M., Huwald, H., Lehning, M., López-Moreno, J.-I., Magnusson, J., Marty, C.,
4 Moran-Tejéda, E., Morin, S., Naaim, M., Provenzale, A., Rabatel, A., Six, D., Stötter, J., Strasser, U.,
5 Terzago, S., and Vincent, C.: The European mountain cryosphere: A review of past, current and future
6 issues, *Alpine Glaciers*, <https://doi.org/10.5194/tc-2016-290>, 2017.

7 Beres, N. D., Sengupta, D., Samburova, V., Khlystov, A. Y., and Moosmüller, H.: Deposition of brown
8 carbon onto snow: changes in snow optical and radiative properties, *Atmos. Chem. Phys.*, 20, 6095–
9 6114, <https://doi.org/10.5194/acp-20-6095-2020>, 2020.

10 Birdwell, J. E. and Engel, A. S.: Characterization of dissolved organic matter in cave and spring waters
11 using UV-Vis absorbance and fluorescence spectroscopy, *Org. Geochem.*, 41, 270–280,
12 <https://doi.org/10.1016/j.orggeochem.2009.11.002>, 2010.

13 Birdwell, J. E. and Valsaraj, K. T.: Characterization of dissolved organic matter in fogwater by excitation-
14 emission matrix fluorescence spectroscopy, *Atmos. Environ.*, 44, 3246–3253,
15 <https://doi.org/10.1016/j.atmosenv.2010.05.055>, 2010.

16 Bond, T. C., Doherty, S. J., Fahey, D. W., Forster, P. M., Berntsen, T., DeAngelo, B. J., Flanner, M. G.,
17 Ghan, S., Kärcher, B., Koch, D., Kinne, S., Kondo, Y., Quinn, P. K., Sarofim, M. C., Schultz, M. G.,
18 Schulz, M., Venkataraman, C., Zhang, H., Zhang, S., Bellouin, N., Guttikunda, S. K., Hopke, P. K.,
19 Jacobson, M. Z., Kaiser, J. W., Klimont, Z., Lohmann, U., Schwarz, J. P., Shindell, D., Storelvmo, T.,
20 Warren, S. G., and Zender, C. S.: Bounding the role of black carbon in the climate system: A scientific
21 assessment, *J. Geophys. Res.-Atmos.*, 118, 5380–5552, <https://doi.org/10.1002/jgrd.50171>, 2013.

22 Browne, E. C., Zhang, X., Franklin, J. P., Ridley, K. J., Kirchstetter, T. W., Wilson, K. R., Cappa, C. D.,

1 and Kroll, J. H.: Effect of heterogeneous oxidative aging on light absorption by biomass burning
2 organic aerosol, *Aerosol Sci. Tech.*, 53, 663–674, <https://doi.org/10.1080/02786826.2019.1599321>,
3 2019.

4 Cao, L., Bala, G., Zheng, M., and Caldeira, K.: Fast and slow climate responses to CO₂ and solar forcing:
5 A linear multivariate regression model characterizing transient climate change, *J. Geophys. Res.-*
6 *Atmos.*, 120, 12,037–12,053, <https://doi.org/10.1002/2015JD023901>, 2015.

7 Chakrabarty, R. K., Moosmüller, H., Chen, L.-W. A., Lewis, K., Arnott, W. P., Mazzoleni, C., Dubey, M.
8 K., Wold, C. E., Hao, W. M., and Kreidenweis, S. M.: Brown carbon in tar balls from smoldering
9 biomass combustion, *Atmos. Chem. Phys.*, 10, 6363–6370, <https://doi.org/10.5194/acp-10-6363-2010>,
10 2010.

11 Chen, Q., Miyazaki, Y., Kawamura, K., Matsumoto, K., Coburn, S., Volkamer, R., Iwamoto, Y., Kagami,
12 S., Deng, Y., Ogawa, S., Ramasamy, S., Kato, S., Ida, A., Kajii, Y., and Mochida, M.: Characterization
13 of Chromophoric Water-Soluble Organic Matter in Urban, Forest, and Marine Aerosols by HR-ToF-
14 AMS Analysis and Excitation-Emission Matrix Spectroscopy, *Environ. Sci. Technol.*, 50, 10351–
15 10360, <https://doi.org/10.1021/acs.est.6b01643>, 2016.

16 Chen, Q., Wang, M., Wang, Y., Zhang, L., Li, Y., and Han, Y.: Oxidative Potential of Water-Soluble
17 Matter Associated with Chromophoric Substances in PM_{2.5} over Xi'an, China, *Environ. Sci. Technol.*,
18 53, 8574–8584, <https://doi.org/10.1021/acs.est.9b01976>, 2019a.

19 Chen, Q., Mu, Z., Song, W., Wang, Y., Yang, Z., Zhang, L., and Zhang, Y.: Size-Resolved
20 Characterization of the Chromophores in Atmospheric Particulate Matter From a Typical Coal-
21 Burning City in China, *J. Geophys. Res. -Atmos.*, 124, 10546–10563,
22 <https://doi.org/10.1029/2019JD031149>, 2019b.

1 Choi, Y., Kanaya, Y., Park, S.-M., Matsuki, A., Sadanaga, Y., Kim, S.-W., Uno, I., Pan, X., Lee, M., Kim,
2 H., and Jung, D. H.: Regional variability in black carbon and carbon monoxide ratio from long-term
3 observations over East Asia: assessment of representativeness for black carbon (BC) and carbon
4 monoxide (CO) emission inventories, *Atmos. Chem. Phys.*, 20, 83–98, [https://doi.org/10.5194/acp-](https://doi.org/10.5194/acp-20-83-2020)
5 20-83-2020, 2020.

6 Coble, P. G.: Characterization of marine and terrestrial DOM in seawater using excitation-emission
7 matrix spectroscopy, *Mar. Chem.*, 51, 325–346, [https://doi.org/10.1016/0304-4203\(95\)00062-3](https://doi.org/10.1016/0304-4203(95)00062-3), 1996.

8 Coble, P. G., Green, S. A., Blough, N. V., and Gagosian, R. B.: Characterization of dissolved organic
9 matter in the Black Sea by fluorescence spectroscopy, *Nature*, 348, 432–435,
10 <https://doi.org/10.1038/348432a0>, 1990.

11 Coble, P. G., Del Castillo, C. E., and Avril, B.: Distribution and optical properties of CDOM in the
12 Arabian Sea during the 1995 Southwest Monsoon, *Deep-Sea Res. Pt. II*, 45, 2195–2223,
13 [https://doi.org/10.1016/S0967-0645\(98\)00068-X](https://doi.org/10.1016/S0967-0645(98)00068-X), 1998.

14 Cui, J., Shi, T., Zhou, Y., Wu, D., Wang, X., and Pu, W.: Satellite-based radiative forcing by light-
15 absorbing particles in snow across the Northern Hemisphere, *Atmos. Chem. Phys.*, 21, 269–288,
16 <https://doi.org/10.5194/acp-21-269-2021>, 2021.

17 Dang, C., Warren, S. G., Fu, Q., Doherty, S. J., Sturm, M., and Su, J.: Measurements of light-absorbing
18 particles in snow across the Arctic, North America, and China: Effects on surface albedo, *J. Geophys.*
19 *Res.-Atmos.*, 122, 10,149–10,168, <https://doi.org/10.1002/2017JD027070>, 2017.

20 Di Mauro, B.: A darker cryosphere in a warming world, *Nat. Clim. Chang.*, 10, 978–979,
21 <https://doi.org/10.1038/s41558-020-0896-8>, 2020.

22 Di Mauro, B., Fava, F., Ferrero, L., Garzonio, R., Baccolo, G., Delmonte, B., and Colombo, R.: Mineral

1 dust impact on snow radiative properties in the European Alps combining ground, UAV, and satellite
2 observations, *J. Geophys. Res.-Atmos.*, 120, 6080–6097, <https://doi.org/10.1002/2015JD023287>,
3 2015.

4 Doherty, S. J., Warren, S. G., Grenfell, T. C., Clarke, A. D., and Brandt, R. E.: Light-absorbing impurities
5 in Arctic snow, *Atmos. Chem. Phys.*, 10, 11647–11680, <https://doi.org/10.5194/acp-10-11647-2010>,
6 2010.

7 Doherty, S. J., Dang, C., Hegg, D. A., Zhang, R., and Warren, S. G.: Black carbon and other light-
8 absorbing particles in snow of central North America: Black carbon in North American snow, *J.*
9 *Geophys. Res.-Atmos.*, 119, 12,807–12,831, <https://doi.org/10.1002/2014JD022350>, 2014.

10 Domine, F.: Air-Snow Interactions and Atmospheric Chemistry, *Science*, 297, 1506–1510,
11 <https://doi.org/10.1126/science.1074610>, 2002.

12 D'Sa, E. J., Goes, J. I., Gomes, H., and Mouw, C.: Absorption and fluorescence properties of
13 chromophoric dissolved organic matter of the eastern Bering Sea in the summer with special reference
14 to the influence of a cold pool, *Biogeosciences*, 11, 3225–3244, [https://doi.org/10.5194/bg-11-3225-](https://doi.org/10.5194/bg-11-3225-2014)
15 2014, 2014.

16 Dumont, M., Brun, E., Picard, G., Michou, M., Libois, Q., Petit, J.-R., Geyer, M., Morin, S., and Josse,
17 B.: Contribution of light-absorbing impurities in snow to Greenland's darkening since 2009, *Nature*
18 *Geosci.*, 7, 509–512, <https://doi.org/10.1038/ngeo2180>, 2014.

19 Els, N., Greilinger, M., Reisecker, M., Tignat-Perrier, R., Baumann-Stanzer, K., Kasper-Giebl, A., Sattler,
20 B., and Larose, C.: Comparison of Bacterial and Fungal Composition and Their Chemical Interaction
21 in Free Tropospheric Air and Snow Over an Entire Winter Season at Mount Sonnblick, Austria, *Front.*
22 *Microbiol.*, 11, <https://doi.org/10.3389/fmicb.2020.00980>, 2020.

1 Fang, L., Bai, Z., Wei, S., Yanfen, H., Zongming, W., Kaishan, S., Dianwei, L., and Zhiming, L.: Sandy
2 desertification change and its driving forces in western Jilin Province, North China, *Environ. Monit.*
3 *Assess.*, 136, 379–390, <https://doi.org/10.1007/s10661-007-9693-3>, 2007.

4 Fellman, J. B., Hood, E., Raymond, P. A., Stubbins, A., and Spencer, R. G. M.: Spatial Variation in the
5 Origin of Dissolved Organic Carbon in Snow on the Juneau Icefield, Southeast Alaska, *Environ. Sci.*
6 *Technol.*, 49, 11492–11499, <https://doi.org/10.1021/acs.est.5b02685>, 2015.

7 Feng, L., Xu, J., Kang, S., Li, X., Li, Y., Jiang, B., and Shi, Q.: Chemical Composition of Microbe-
8 Derived Dissolved Organic Matter in Cryoconite in Tibetan Plateau Glaciers: Insights from Fourier
9 Transform Ion Cyclotron Resonance Mass Spectrometry Analysis, *Environ. Sci. Technol.*, 50, 13215–
10 13223, <https://doi.org/10.1021/acs.est.6b03971>, 2016.

11 Feng, L., An, Y., Xu, J., and Kang, S.: Characteristics and sources of dissolved organic matter in a glacier
12 in the northern Tibetan Plateau: differences between different snow categories, *Ann. Glaciol.*, 59, 31–
13 40, <https://doi.org/10.1017/aog.2018.20>, 2018.

14 Flanner, M. G., Zender, C. S., Randerson, J. T., and Rasch, P. J.: Present-day climate forcing and response
15 from black carbon in snow, *J. Geophys. Res.*, 112, D11202, <https://doi.org/10.1029/2006JD008003>,
16 2007.

17 Fu, P., Kawamura, K., Chen, J., Qin, M., Ren, L., Sun, Y., Wang, Z., Barrie, L. A., Tachibana, E., Ding,
18 A., and Yamashita, Y.: Fluorescent water-soluble organic aerosols in the High Arctic atmosphere, *Sci.*
19 *Rep.*, 5, 9845, <https://doi.org/10.1038/srep09845>, 2015.

20 Grannas, A. M., Jones, A. E., Dibb, J., Ammann, M., Anastasio, C., Beine, H. J., Bergin, M., Bottenheim,
21 J., Boxe, C. S., Carver, G., Chen, G., Crawford, J. H., Domine, F., Frey, M. M., Guzman, M. I., Heard,
22 D. E., Helmig, D., Hoffmann, M. R., Honrath, R. E., Huey, L. G., Hutterli, M., Jacobi, H. W., Klan, P.,

1 Lefer, B., McConnell, J., Plane, J., Sander, R., Savarino, J., Shepson, P. B., Simpson, W. R., Sodeau,
2 J. R., Weller, R., Wolff, E. W., and Zhu, T.: An overview of snow photochemistry: evidence,
3 mechanisms and impacts, *Atmos. Chem. Phys.*, 45, <https://doi.org/10/fjqs2v>, 2007.

4 Groisman, P. Ya., Karl, T. R., and Knight, R. W.: Observed Impact of Snow Cover on the Heat Balance
5 and the Rise of Continental Spring Temperatures, *Science*, 263, 198–200,
6 <https://doi.org/10.1126/science.263.5144.198>, 1994.

7 Guo, B., Li, W., Santibáñez, P., Priscu, J. C., Liu, Y., and Liu, K.: Organic matter distribution in the icy
8 environments of Taylor Valley, Antarctica, *Sci. Total Environ.*, 841, 156639,
9 <https://doi.org/10.1016/j.scitotenv.2022.156639>, 2022.

10 Guo, J. and Hu, Y.: Spatiotemporal Variations in Satellite-Derived Vegetation Phenological Parameters
11 in Northeast China, *Remote Sen.*, 14, 705, <https://doi.org/10.3390/rs14030705>, 2022.

12 Gustafsson, Ö., Kruså, M., Zencak, Z., Sheesley, R. J., Granat, L., Engström, E., Praveen, P. S., Rao, P.
13 S. P., Leck, C., and Rodhe, H.: Brown Clouds over South Asia: Biomass or Fossil Fuel Combustion?,
14 *Science*, 323, 495–498, <https://doi.org/10.1126/science.1164857>, 2009.

15 Hansen, J. and Nazarenko, L.: Soot climate forcing via snow and ice albedos, *P. Natl. Acad. Sci. USA*,
16 101, 423–428, <https://doi.org/10.1073/pnas.2237157100>, 2004.

17 Hegg, D. A., Warren, S. G., Grenfell, T. C., Sarah J Doherty, and Clarke, A. D.: Sources of light-absorbing
18 aerosol in Arctic snow and their seasonal variation, *Atmos. Chem. Phys.*, 10, 10923–10938,
19 <https://doi.org/10.5194/acp-10-10923-2010>, 2010.

20 Helms, J. R., Stubbins, A., Perdue, E. M., Green, N. W., Chen, H., and Mopper, K.: Photochemical
21 bleaching of oceanic dissolved organic matter and its effect on absorption spectral slope and
22 fluorescence, *Mar. Chem.*, 155, 81–91, <https://doi.org/10.1016/j.marchem.2013.05.015>, 2013.

1 Hood, E., Battin, T. J., Fellman, J., O'Neel, S., and Spencer, R. G. M.: Storage and release of organic
2 carbon from glaciers and ice sheets, *Nature Geosci.*, 8, 91–96, <https://doi.org/10.1038/ngeo2331>, 2015.

3 Hotaling, S., Lutz, S., Dial, R. J., Anesio, A. M., Benning, L. G., Fountain, A. G., Kelley, J. L.,
4 McCutcheon, J., Skiles, S. M., Takeuchi, N., and Hamilton, T. L.: Biological albedo reduction on ice
5 sheets, glaciers, and snowfields, *Earth-Sci. Rev.*, 220, 103728,
6 <https://doi.org/10.1016/j.earscirev.2021.103728>, 2021.

7 Huang, J., Fu, Q., Zhang, W., Wang, X., Zhang, R., Ye, H., and Warren, S. G.: Dust and Black Carbon in
8 Seasonal Snow Across Northern China, *Bull. Amer. Meteor. Soc.*, 92, 175–181,
9 <https://doi.org/10.1175/2010BAMS3064.1>, 2011.

10 Huguet, A., Vacher, L., Relexans, S., Saubusse, S., Froidefond, J. M., and Parlanti, E.: Properties of
11 fluorescent dissolved organic matter in the Gironde Estuary, *Org. Geochem.*, 40, 706–719,
12 <https://doi.org/10.1016/j.orggeochem.2009.03.002>, 2009.

13 Kirillova, E. N., Andersson, A., Han, J., Lee, M., and Gustafsson, Ö.: Sources and light absorption of
14 water-soluble organic carbon aerosols in the outflow from northern China, *Atmos. Chem. Phys.*, 14,
15 1413–1422, <https://doi.org/10.5194/acp-14-1413-2014>, 2014.

16 Kothawala, D. N., Murphy, K. R., Stedmon, C. A., Weyhenmeyer, G. A., and Tranvik, L. J.: Inner filter
17 correction of dissolved organic matter fluorescence: Correction of inner filter effects, *Limnol.*
18 *Oceanogr-Meth.*, 11, 616–630, <https://doi.org/10.4319/lom.2013.11.616>, 2013.

19 Kowalczyk, P., Stoń-Egiert, J., Cooper, W. J., Whitehead, R. F., and Durako, M. J.: Characterization of
20 chromophoric dissolved organic matter (CDOM) in the Baltic Sea by excitation emission matrix
21 fluorescence spectroscopy, *Mar. Chem.*, 96, 273–292, <https://doi.org/10.1016/j.marchem.2005.03.002>,
22 2005.

1 Lawaetz, A. J. and Stedmon, C. A.: Fluorescence Intensity Calibration Using the Raman Scatter Peak of
2 Water, *Appl. Spectrosc.*, 63, 936–940, <https://doi.org/10.1366/000370209788964548>, 2009.

3 Li, C., Yan, F., Kang, S., Yan, C., Hu, Z., Chen, P., Gao, S., Zhang, C., He, C., Kaspari, S., and Stubbins,
4 A.: Carbonaceous matter in the atmosphere and glaciers of the Himalayas and the Tibetan plateau: An
5 investigative review, *Environ. Int.*, 146, 106281, <https://doi.org/10.1016/j.envint.2020.106281>, 2021a.

6 Li, X., Fu, P., Tripathee, L., Yan, F., Hu, Z., Yu, F., Chen, Q., Li, J., Chen, Q., Cao, J., and Kang, S.:
7 Molecular compositions, optical properties, and implications of dissolved brown carbon in snow/ice
8 on the Tibetan Plateau glaciers, *Environ. Int.*, 164, 107276,
9 <https://doi.org/10.1016/j.envint.2022.107276>, 2022.

10 Li, Y., Kang, S., Zhang, X., Chen, J., Schmale, J., Li, X., Zhang, Y., Niu, H., Li, Z., Qin, X., He, X., Yang,
11 W., Zhang, G., Wang, S., Shao, L., and Tian, L.: Black carbon and dust in the Third Pole glaciers:
12 Revaluated concentrations, mass absorption cross-sections and contributions to glacier ablation, *Sci.*
13 *Total Environ.*, 789, 147746, <https://doi.org/10.1016/j.scitotenv.2021.147746>, 2021b.

14 Lu, Z., Zhang, Q., and Streets, D. G.: Sulfur dioxide and primary carbonaceous aerosol emissions in
15 China and India, 1996–2010, *Atmos. Chem. Phys.*, 11, 9839–9864, [https://doi.org/10.5194/acp-11-](https://doi.org/10.5194/acp-11-9839-2011)
16 [9839-2011](https://doi.org/10.5194/acp-11-9839-2011), 2011.

17 McKnight, D. M., Boyer, E. W., Westerhoff, P. K., Doran, P. T., Kulbe, T., and Andersen, D. T.:
18 Spectrofluorometric characterization of dissolved organic matter for indication of precursor organic
19 material and aromaticity, *Limnol. Oceanogr.*, 46, 38–48, <https://doi.org/10.4319/lo.2001.46.1.0038>,
20 2001.

21 McNeill, V. F., Grannas, A. M., Abbatt, J. P. D., Ammann, M., Ariya, P., Bartels-Rausch, T., Domine, F.,
22 Donaldson, D. J., Guzman, M. I., Heger, D., Kahan, T. F., Klán, P., Masclin, S., Toubin, C., and Voisin,

1 D.: Organics in environmental ices: sources, chemistry, and impacts, *Atmos. Chem. Phys.*, 12, 9653–
2 9678, <https://doi.org/10.5194/acp-12-9653-2012>, 2012.

3 Meyer, T. and Wania, F.: Organic contaminant amplification during snowmelt, *Water Res.*, 42, 1847–
4 1865, <https://doi.org/10.1016/j.watres.2007.12.016>, 2008.

5 Mladenov, N., Alados-Arboledas, L., Olmo, F. J., Lyamani, H., Delgado, A., Molina, A., and Reche, I.:
6 Applications of optical spectroscopy and stable isotope analyses to organic aerosol source
7 discrimination in an urban area, *Atmos. Environ.*, 45, 1960–1969,
8 <https://doi.org/10.1016/j.atmosenv.2011.01.029>, 2011.

9 Murphy, K. R., Stedmon, C. A., Waite, T. D., and Ruiz, G. M.: Distinguishing between terrestrial and
10 autochthonous organic matter sources in marine environments using fluorescence spectroscopy, *Mar.*
11 *Chem.*, 108, 40–58, <https://doi.org/10.1016/j.marchem.2007.10.003>, 2008.

12 Murphy, K. R., Hambly, A., Singh, S., Henderson, R. K., Baker, A., Stuetz, R., and Khan, S. J.: Organic
13 Matter Fluorescence in Municipal Water Recycling Schemes: Toward a Unified PARAFAC Model,
14 *Environ. Sci. Technol.*, 45, 2909–2916, <https://doi.org/10.1021/es103015e>, 2011.

15 Murphy, K. R., Stedmon, C. A., Graeber, D., and Bro, R.: Fluorescence spectroscopy and multi-way
16 techniques. PARAFAC, *Anal. Methods*, 5, 6557, <https://doi.org/10.1039/c3ay41160e>, 2013.

17 Niu, H., Kang, S., Lu, X., and Shi, X.: Distributions and light absorption property of water soluble organic
18 carbon in a typical temperate glacier, southeastern Tibetan Plateau, *Tellus B*, 70, 1–15,
19 <https://doi.org/10.1080/16000889.2018.1468705>, 2018.

20 Ohno, T.: Fluorescence Inner-Filtering Correction for Determining the Humification Index of Dissolved
21 Organic Matter, *Environ. Sci. Technol.*, 36, 742–746, <https://doi.org/10.1021/es0155276>, 2002.

22 Osburn, C. L., Handsel, L. T., Peierls, B. L., and Paerl, H. W.: Predicting Sources of Dissolved Organic

1 Nitrogen to an Estuary from an Agro-Urban Coastal Watershed, *Environ. Sci. Technol.*, 50, 8473–8484,
2 <https://doi.org/10.1021/acs.est.6b00053>, 2016.

3 Painter, T. H., Barrett, A. P., Landry, C. C., Neff, J. C., Cassidy, M. P., Lawrence, C. R., McBride, K. E.,
4 and Farmer, G. L.: Impact of disturbed desert soils on duration of mountain snow cover, *Geophys. Res.*
5 *Let.*, 34, L12502, <https://doi.org/10.1029/2007GL030284>, 2007.

6 Painter, T. H., Seidel, F. C., Bryant, A. C., McKenzie Skiles, S., and Rittger, K.: Imaging spectroscopy
7 of albedo and radiative forcing by light-absorbing impurities in mountain snow, *J. Geophys. Res.-*
8 *Atmos.*, 118, 9511–9523, <https://doi.org/10.1002/jgrd.50520>, 2013.

9 Pokrovsky, O. M.: Quantitative Estimates of the Impact of the Most Important Factors on Global Climate
10 Change over the Past 150 Years, *Izv. Atmos. Ocean. Phys.*, 55, 1182–1188,
11 <https://doi.org/10.1134/S0001433819090354>, 2019.

12 Pu, W., Wang, X., Wei, H., Zhou, Y., Shi, J., Hu, Z., Jin, H., and Chen, Q.: Properties of black carbon and
13 other insoluble light-absorbing particles in seasonal snow of northwestern China, *The Cryosphere*, 11,
14 1213–1233, <https://doi.org/10.5194/tc-11-1213-2017>, 2017.

15 Pu, W., Cui, J., Shi, T., Zhang, X., He, C., and Wang, X.: The remote sensing of radiative forcing by
16 light-absorbing particles (LAPs) in seasonal snow over northeastern China, *Atmos. Chem. Phys.*, 19,
17 9949–9968, <https://doi.org/10.5194/acp-19-9949-2019>, 2019.

18 Pu, W., Shi, T., Cui, J., Chen, Y., Zhou, Y., and Wang, X.: Enhancement of snow albedo reduction and
19 radiative forcing due to coated black carbon in snow, *The Cryosphere*, 15, 2255–2272,
20 <https://doi.org/10.5194/tc-15-2255-2021>, 2021.

21 Qian, Y., Yasunari, T. J., Doherty, S. J., Flanner, M. G., Lau, W. K. M., Ming, J., Wang, H., Wang, M.,
22 Warren, S. G., and Zhang, R.: Light-absorbing particles in snow and ice: Measurement and modeling

1 of climatic and hydrological impact, *Adv. Atmos. Sci.*, 32, 64–91, [https://doi.org/10.1007/s00376-014-](https://doi.org/10.1007/s00376-014-0010-0)
2 0010-0, 2015.

3 Ram, K., Sarin, M. M., and Hegde, P.: Long-term record of aerosol optical properties and chemical
4 composition from a high-altitude site (Manora Peak) in Central Himalaya, *Atmos. Chem. Phys.*, 10,
5 11791–11803, <https://doi.org/10.5194/acp-10-11791-2010>, 2010.

6 Sarangi, C., Qian, Y., Rittger, K., Ruby Leung, L., Chand, D., Bormann, K. J., and Painter, T. H.: Dust
7 dominates high-altitude snow darkening and melt over high-mountain Asia, *Nat. Clim. Chang.*, 10,
8 1045–1051, <https://doi.org/10.1038/s41558-020-00909-3>, 2020.

9 Seekell, D. A., Lapierre, J.-F., Ask, J., Bergström, A.-K., Deininger, A., Rodríguez, P., and Karlsson, J.:
10 The influence of dissolved organic carbon on primary production in northern lakes, *Limnol. Oceanogr.*,
11 60, 1276–1285, <https://doi.org/10.1002/lno.10096>, 2015.

12 Shamjad, P. M., Tripathi, S. N., Thamban, N. M., and Vreeland, H.: Refractive Index and Absorption
13 Attribution of Highly Absorbing Brown Carbon Aerosols from an Urban Indian City-Kanpur, *Sci. Rep.*,
14 6, 37735, <https://doi.org/10.1038/srep37735>, 2016.

15 Shi, T., Pu, W., Zhou, Y., Cui, J., Zhang, D., and Wang, X.: Albedo of Black Carbon-Contaminated Snow
16 Across Northwestern China and the Validation With Model Simulation, *J. Geophys. Res.-Atmos.*, 125,
17 e2019JD032065, <https://doi.org/10.1029/2019JD032065>, 2020.

18 Shi, T., Cui, J., Chen, Y., Zhou, Y., Pu, W., Xu, X., Chen, Q., Zhang, X., and Wang, X.: Enhanced light
19 absorption and reduced snow albedo due to internally mixed mineral dust in grains of snow, *Atmos.*
20 *Chem. Phys.*, 21, 6035–6051, <https://doi.org/10.5194/acp-21-6035-2021>, 2021.

21 Shi, T., Chen, Y., Xing, Y., Niu, X., Wu, D., Cui, J., Zhou, Y., Pu, W., and Wang, X.: Assessment of the
22 combined radiative effects of black carbon in the atmosphere and snowpack in the Northern

1 Hemisphere constrained by surface observations, *Environ. Sci.: Atmos.*, 2, 702–713,
2 <https://doi.org/10.1039/D2EA00005A>, 2022a.

3 Shi, T., Cui, J., Wu, D., Xing, Y., Chen, Y., Zhou, Y., Pu, W., and Wang, X.: Snow albedo reductions
4 induced by the internal/external mixing of black carbon and mineral dust, and different snow grain
5 shapes across northern China, *Environ. Res.*, 208, 112670,
6 <https://doi.org/10.1016/j.envres.2021.112670>, 2022b.

7 Singer, G. A., Fasching, C., Wilhelm, L., Niggemann, J., Steier, P., Dittmar, T., and Battin, T. J.:
8 Biogeochemically diverse organic matter in Alpine glaciers and its downstream fate, *Nature Geosci.*,
9 5, 710–714, <https://doi.org/10.1038/ngeo1581>, 2012.

10 Skiles, S. M., Flanner, M., Cook, J. M., Dumont, M., and Painter, T. H.: Radiative forcing by light-
11 absorbing particles in snow, *Nat. Clim. Change*, 8, 964–971, [https://doi.org/10.1038/s41558-018-](https://doi.org/10.1038/s41558-018-0296-5)
12 [0296-5](https://doi.org/10.1038/s41558-018-0296-5), 2018.

13 Song, K., Shang, Y., Wen, Z., Jacinthe, P.-A., Liu, G., Lyu, L., and Fang, C.: Characterization of CDOM
14 in saline and freshwater lakes across China using spectroscopic analysis, *Water Res.*, 150, 403–417,
15 <https://doi.org/10.1016/j.watres.2018.12.004>, 2019.

16 Stedmon, C. A. and Markager, S.: Resolving the variability in dissolved organic matter fluorescence in a
17 temperate estuary and its catchment using PARAFAC analysis, *Limnol. Oceanogr.*, 50, 686–697,
18 <https://doi.org/10.4319/lo.2005.50.2.0686>, 2005.

19 Stedmon, C. A., Markager, S., and Bro, R.: Tracing dissolved organic matter in aquatic environments
20 using a new approach to fluorescence spectroscopy, *Mar. Chem.*, 82, 239–254,
21 [https://doi.org/10.1016/S0304-4203\(03\)00072-0](https://doi.org/10.1016/S0304-4203(03)00072-0), 2003.

22 Stedmon, C. A., Thomas, D. N., Granskog, M., Kaartokallio, H., Papadimitriou, S., and Kuosa, H.:

1 Characteristics of Dissolved Organic Matter in Baltic Coastal Sea Ice: Allochthonous or
2 Autochthonous Origins?, *Environ. Sci. Technol.*, 41, 7273–7279, <https://doi.org/10.1021/es071210f>,
3 2007.

4 Usha, K. H., Nair, V. S., and Babu, S. S.: Modeling of aerosol induced snow albedo feedbacks over the
5 Himalayas and its implications on regional climate, *Clim. Dynam.*, 54, 4191–4210,
6 <https://doi.org/10.1007/s00382-020-05222-5>, 2020.

7 Vione, D., Colombo, N., Said-Pullicino, D., Bocchiola, D., Confortola, G., Salerno, F., Viviano, G.,
8 Fratianni, S., Martin, M., Godone, D., and Freppaz, M.: Seasonal variations in the optical
9 characteristics of dissolved organic matter in glacial pond water, *Sci. Total Environ.*, 759, 143464,
10 <https://doi.org/10.1016/j.scitotenv.2020.143464>, 2021.

11 Voisin, D., Jaffrezo, J.-L., Houdier, S., Barret, M., Cozic, J., King, M. D., France, J. L., Reay, H. J.,
12 Grannas, A., Kos, G., Ariya, P. A., Beine, H. J., and Domine, F.: Carbonaceous species and humic like
13 substances (HULIS) in Arctic snowpack during OASIS field campaign in Barrow, *J. Geophys. Res.*,
14 117, <https://doi.org/10.1029/2011JD016612>, 2012.

15 Wang, J., Wang, Y., Yan, C., and Qi, Y.: 1:100,000 desert (sand) distribution dataset in China, edited by:
16 National Tibetan Plateau Data Center, National Tibetan Plateau Data Center,
17 <https://doi.org/10.3972/westdc.006.2013.db>, 2013a.

18 Wang, R., Tao, S., Balkanski, Y., Ciais, P., Boucher, O., Liu, J., Piao, S., Shen, H., Vuolo, M. R., Valari,
19 M., Chen, H., Chen, Y., Cozic, A., Huang, Y., Li, B., Li, W., Shen, G., Wang, B., and Zhang, Y.:
20 Exposure to ambient black carbon derived from a unique inventory and high-resolution model, *P. Natl.*
21 *Acad. Sci. USA*, 111, 2459–2463, <https://doi.org/10.1073/pnas.1318763111>, 2014a.

22 Wang, X., Doherty, S. J., and Huang, J.: Black carbon and other light-absorbing impurities in snow across

1 Northern China, *J. Geophys. Res.-Atmos.*, 118, 1471–1492, <https://doi.org/10.1029/2012JD018291>,

2 2013b.

3 Wang, X., Xu, B., and Ming, J.: An overview of the studies on black carbon and mineral dust deposition

4 in snow and ice cores in East Asia, *J. Meteorol. Res.*, 28, 354–370, [https://doi.org/10.1007/s13351-](https://doi.org/10.1007/s13351-014-4005-7)

5 014-4005-7, 2014b.

6 Wang, X., Pu, W., Zhang, X., Ren, Y., and Huang, J.: Water-soluble ions and trace elements in surface

7 snow and their potential source regions across northeastern China, *Atmos. Environ.*, 114, 57–65,

8 <https://doi.org/10.1016/j.atmosenv.2015.05.012>, 2015.

9 Wang, X., Pu, W., Ren, Y., Zhang, X., Zhang, X., Shi, J., Jin, H., Dai, M., and Chen, Q.: Observations

10 and model simulations of snow albedo reduction in seasonal snow due to insoluble light-absorbing

11 particles during 2014 Chinese survey, *Atmos. Chem. Phys.*, 17, 2279–2296,

12 <https://doi.org/10.5194/acp-17-2279-2017>, 2017.

13 Wang, X., Bai, X., Ma, L., He, C., Jiang, H., Sheng, L., and Luo, W.: Snow depths' impact on soil

14 microbial activities and carbon dioxide fluxes from a temperate wetland in Northeast China, *Sci. Rep.*,

15 10, 8709, <https://doi.org/10.1038/s41598-020-65569-x>, 2020.

16 Warren, S. and Wiscombe, W.: A Model for the Spectral Albedo of Snow. II: Snow Containing

17 Atmospheric Aerosols, *J. Atmos. Sci.*, 37, 2734–2745, [https://doi.org/10.1175/1520-](https://doi.org/10.1175/1520-0469(1980)037<2734:AMFTSA>2.0.CO;2)

18 0469(1980)037<2734:AMFTSA>2.0.CO;2, 1980.

19 Wen, H., Zhou, Y., Xu, X., Wang, T., Chen, Q., Chen, Q., Li, W., Wang, Z., Huang, Z., Zhou, T., Shi, J.,

20 Bi, J., Ji, M., and Wang, X.: Water-soluble brown carbon in atmospheric aerosols along the transport

21 pathway of Asian dust: Optical properties, chemical compositions, and potential sources, *Sci. Total*

22 *Environ.*, 789, 147971, <https://doi.org/10.1016/j.scitotenv.2021.147971>, 2021.

1 Wu, D., Liu, J., Wang, T., Niu, X., Chen, Z., Wang, D., Zhang, X., Ji, M., Wang, X., and Pu, W.: Applying
2 a dust index over North China and evaluating the contribution of potential factors to its distribution,
3 *Atmos. Res.*, 254, 105515, <https://doi.org/10.1016/j.atmosres.2021.105515>, 2021.

4 Wu, D., Shi, T., Niu, X., Chen, Z., Cui, J., Chen, Y., Zhang, X., Liu, J., Ji, M., Wang, X., and Pu, W.:
5 Seasonal to sub-seasonal variations of the Asian Tropopause Aerosols Layer affected by the deep
6 convection, surface pollutants and precipitation, *J. Environ. Sci.*, 114, 53–65,
7 <https://doi.org/10.1016/j.jes.2021.07.022>, 2022.

8 Wu, G., Ram, K., Fu, P., Wang, W., Zhang, Y., Liu, X., Stone, E. A., Pradhan, B. B., Dangol, P. M.,
9 Panday, A. K., Wan, X., Bai, Z., Kang, S., Zhang, Q., and Cong, Z.: Water-Soluble Brown Carbon in
10 Atmospheric Aerosols from Godavari (Nepal), a Regional Representative of South Asia, *Environ. Sci.*
11 *Technol.*, 53, 3471–3479, <https://doi.org/10.1021/acs.est.9b00596>, 2019.

12 Wu, G., Wan, X., Ram, K., Li, P., Liu, B., Yin, Y., Fu, P., Loewen, M., Gao, S., Kang, S., Kawamura, K.,
13 Wang, Y., and Cong, Z.: Light absorption, fluorescence properties and sources of brown carbon
14 aerosols in the Southeast Tibetan Plateau, *Environ. Pollut.*, 257, 113616,
15 <https://doi.org/10.1016/j.envpol.2019.113616>, 2020.

16 Wu, G., Cong, Z., Kang, S., Kawamura, K., Fu, P., Zhang, Y., Wan, X., Gao, S., and Liu, B.: Brown
17 carbon in the cryosphere: Current knowledge and perspective, *Adv. Clim. Chang. Res.*, 7, 82–89,
18 <https://doi.org/10.1016/j.accre.2016.06.002>, 2016.

19 Xie, X., Liu, X., Che, H., Xie, X., Li, X., Shi, Z., Wang, H., Zhao, T., and Liu, Y.: Radiative feedbacks
20 of dust in snow over eastern Asia in CAM4-BAM, *Atmos. Chem. Phys.*, 18, 12683–12698,
21 <https://doi.org/10.5194/acp-18-12683-2018>, 2018.

22 Xin, J., Gong, C., Liu, Z., Cong, Z., Gao, W., Song, T., Pan, Y., Sun, Y., Ji, D., Wang, L., Tang, G., and

1 Wang, Y.: The observation-based relationships between PM_{2.5} and AOD over China, *J. Geophys. Res.-*
2 *Atmos.*, 121, 10,701-10,716, <https://doi.org/10.1002/2015JD024655>, 2016.

3 Yamashita, Y., Jaffé, R., Maie, N., and Tanoue, E.: Assessing the dynamics of dissolved organic matter
4 (DOM) in coastal environments by excitation emission matrix fluorescence and parallel factor analysis
5 (EEM-PARAFAC), *Limnol. Oceanogr.*, 53, 1900–1908, <https://doi.org/10.4319/lo.2008.53.5.1900>,
6 2008.

7 Yan, F., Kang, S., Li, C., Zhang, Y., Qin, X., Li, Y., Zhang, X., Hu, Z., Chen, P., Li, X., Qu, B., and
8 Sillanpää, M.: Concentration, sources and light absorption characteristics of dissolved organic carbon
9 on a medium-sized valley glacier, northern Tibetan Plateau, *The Cryosphere*, 10, 2611–2621,
10 <https://doi.org/10.5194/tc-10-2611-2016>, 2016.

11 Zatko, M. C., Grenfell, T. C., Alexander, B., Doherty, S. J., Thomas, J. L., and Yang, X.: The influence
12 of snow grain size and impurities on the vertical profiles of actinic flux and associated NO_x emissions
13 on the Antarctic and Greenland ice sheets, *Atmos. Chem. Phys.*, 13, 3547–3567,
14 <https://doi.org/10.5194/acp-13-3547-2013>, 2013.

15 Zhang, R., Hegg, D. A., Huang, J., and Fu, Q.: Source attribution of insoluble light-absorbing particles
16 in seasonal snow across northern China, *Atmos. Chem. Phys.*, 13, 6091–6099,
17 <https://doi.org/10.5194/acp-13-6091-2013>, 2013.

18 Zhang, Y., van Dijk, M. A., Liu, M., Zhu, G., and Qin, B.: The contribution of phytoplankton degradation
19 to chromophoric dissolved organic matter (CDOM) in eutrophic shallow lakes: Field and experimental
20 evidence, *Water Res.*, 43, 4685–4697, <https://doi.org/10.1016/j.watres.2009.07.024>, 2009.

21 Zhang, Y., Kang, S., Cong, Z., Schmale, J., Sprenger, M., Li, C., Yang, W., Gao, T., Sillanpää, M., Li, X.,
22 Liu, Y., Chen, P., and Zhang, X.: Light-absorbing impurities enhance glacier albedo reduction in the

1 southeastern Tibetan plateau: Light-Absorbing Impurities in Snow, *J. Geophys. Res.-Atmos.*, 122,
2 6915–6933, <https://doi.org/10.1002/2016JD026397>, 2017.

3 Zhang, Y., Kang, S., Sprenger, M., Cong, Z., Gao, T., Li, C., Tao, S., Li, X., Zhong, X., Xu, M., Meng,
4 W., Neupane, B., Qin, X., and Sillanpää, M.: Black carbon and mineral dust in snow cover on the
5 Tibetan Plateau, *The Cryosphere*, 12, 413–431, <https://doi.org/10.5194/tc-12-413-2018>, 2018.

6 Zhang, Y., Kang, S., Gao, T., Sprenger, M., Dou, T., Han, W., Zhang, Q., Sun, S., Du, W., Chen, P., Guo,
7 J., Cui, X., and Sillanpää, M.: Dissolved organic carbon in Alaskan Arctic snow: concentrations, light-
8 absorption properties, and bioavailability, *Tellus B*, 72, 1–19,
9 <https://doi.org/10.1080/16000889.2020.1778968>, 2020.

10 Zhao, C., Hu, Z., Qian, Y., Ruby Leung, L., Huang, J., Huang, M., Jin, J., Flanner, M. G., Zhang, R.,
11 Wang, H., Yan, H., Lu, Z., and Streets, D. G.: Simulating black carbon and dust and their radiative
12 forcing in seasonal snow: a case study over North China with field campaign measurements, *Atmos.*
13 *Chem. Phys.*, 14, 11475–11491, <https://doi.org/10.5194/acp-14-11475-2014>, 2014.

14 Zhao, Y., Xu, X., Huang, W., Wang, Y., Xu, Y., Chen, H., and Kang, Z.: Trends in observed mean and
15 extreme precipitation within the Yellow River Basin, China, *Theor. Appl. Climatol.*, 136, 1387–1396,
16 <https://doi.org/10.1007/s00704-018-2568-4>, 2019.

17 Zhou, L., Zhou, Y., Hu, Y., Cai, J., Liu, X., Bai, C., Tang, X., Zhang, Y., Jang, K.-S., Spencer, R. G. M.,
18 and Jeppesen, E.: Microbial production and consumption of dissolved organic matter in glacial
19 ecosystems on the Tibetan Plateau, *Water Res.*, 160, 18–28,
20 <https://doi.org/10.1016/j.watres.2019.05.048>, 2019a.

21 Zhou, Y., Shi, K., Zhang, Y., Jeppesen, E., Liu, X., Zhou, Q., Wu, H., Tang, X., and Zhu, G.: Fluorescence
22 peak integration ratio IC:IT as a new potential indicator tracing the compositional changes in

1 chromophoric dissolved organic matter, *Sci. Total Environ.*, 574, 1588–1598,
2 <https://doi.org/10.1016/j.scitotenv.2016.08.196>, 2017.

3 Zhou, Y., Wen, H., Liu, J., Pu, W., Chen, Q., and Wang, X.: The optical characteristics and sources of
4 chromophoric dissolved organic matter (CDOM) in seasonal snow of northwestern China, *The*
5 *Cryosphere*, 13, 157–175, <https://doi.org/10.5194/tc-13-157-2019>, 2019b.

6 Zhou, Y., West, C. P., Hettiyadura, A. P. S., Niu, X., Wen, H., Cui, J., Shi, T., Pu, W., Wang, X., and
7 Laskin, A.: Measurement report: Molecular composition, optical properties, and radiative effects of
8 water-soluble organic carbon in snowpack samples from northern Xinjiang, China, *Atmos. Chem.*
9 *Phys.*, 21, 8531–8555, <https://doi.org/10.5194/acp-21-8531-2021>, 2021.

10 Zhou, Y., West, C. P., Hettiyadura, A. P. S., Pu, W., Shi, T., Niu, X., Wen, H., Cui, J., Wang, X., and
11 Laskin, A.: Molecular Characterization of Water-Soluble Brown Carbon Chromophores in Snowpack
12 from Northern Xinjiang, China, *Environ. Sci. Technol.*, [acs.est.1c07972](https://doi.org/10.1021/acs.est.1c07972),
13 <https://doi.org/10.1021/acs.est.1c07972>, 2022.

14 Zsolnay, A., Baigar, E., Jimenez, M., Steinweg, B., and Saccomandi, F.: Differentiating with fluorescence
15 spectroscopy the sources of dissolved organic matter in soils subjected to drying, *Chemosphere*, 38, 45–
16 50, [https://doi.org/10.1016/S0045-6535\(98\)00166-0](https://doi.org/10.1016/S0045-6535(98)00166-0), 1999.